FEATURE ARTICLE

Semiconductor Nanowires for Subwavelength Photonics Integration

Donald J. Sirbuly, Matt Law, Haoquan Yan, and Peidong Yang*

Department of Chemistry, University of California, Berkeley, Berkeley, California 94720, and Materials Sciences Division, Lawrence Berkeley National Laboratory, 1 Cyclotron Road, Berkeley, California 94720

This article focuses on one-dimensional (1D) semiconductor subwavelength optical elements and assesses their potential use as active and passive components in photonic devices. An updated overview of their optical properties, including spontaneous emission, ultrafast carrier dynamics, cavity resonance feedback (lasing), photodetection, and waveguiding, is provided. The ability to physically manipulate these structures on surfaces to form simple networks and assemblies is the first step toward integrating chemically synthesized nanomaterials into photonic circuitry. These high index semiconductor nanowires are capable of efficiently guiding light through liquid media, suggesting a role for such materials in microfluidics-based biosensing applications.

1. Introduction

As information processing approaches the bandwidth limits of silicon-based electronic devices, new technologies will emerge which offer the low cost, low power, and high-speed signaling necessary for future communication and computing platforms. Since transfer rates exceeding 1 Gb/s strain even the fastest state-of-the-art electronic designs, it is appropriate to focus on optical manipulation as an alternative means to rapidly transfer information. Photonic devices utilize photons rather than electrons to carry out logic operations by integrating a number of optical components,[1] each having specific functionality.[2] One requirement of this approach is the ability to trap photons in small volumes so they may be used as data carriers, in analogy to electrons in transistors. Preferably this confinement would occur in structures with dimensions much smaller than the free space wavelength of the propagating light wave (i.e., in subwavelength structures). Many recent systems, such as photonic crystals,[3−7] high dielectric materials,[8] and plasmonics,[9−11] have demonstrated advances in this area. However, production of these structures remains costly and labor intensive. An alternative approach to these elaborately engineered materials is to synthesize nanostructures that intrinsically provide the desired optical and electronic properties to generate, route and detect light on a fully integrated optical chip.

In comparison to their highly studied 0-dimensional (quantum dots)[12−15] and 2-dimensional (quantum wells)[16−19] counterparts, 1-dimensional nanostructures have only recently been the focus of intense research.[20−22] The fabrication of nanoscale structures has been carried out by a host of top-down techniques such as nanolithography (electron and focused-ion-beam),[23−25] proximal-probe patterning,[26,27] and extreme UV or X-ray lithography.[28,29] The main drawbacks to these conventional schemes, however, include the low product yield, limited flexibility in material composition, elevated costs, and the fact that the processing steps tend to be long and rigorous. Bottom-up processes such as chemical synthesis, which include solution-based and gas-phase syntheses, have now begun to compete with the traditional approaches to producing high quality optical elements for device integration. Materials produced through gas-phase chemistry will be highlighted in this review since their optical and electronic properties have been well studied over the past few years.

One-dimensional nanomaterials are promising candidates for photonics integration due to their intriguing optical, electronic, and mechanical properties.[30] Semiconductor systems with photon, phonon and/or electron confinement in two dimensions offer a distinct way to study electrical, thermal, mechanical, and optical phenomena as a function of dimensionality and size reduction. These structures have cross-sectional dimensions that can be tuned from 5 to 500 nm, with lengths spanning hundreds of nanometers to millimeters. One-dimensional nanomaterials can also be synthesized as specific functioning optical components (i.e., actives and passives) in an optical system. The assortment of nanowire optical and electronic devices now includes transistors and logic gates,[31−33] photodetectors,[34,35] chemical and gas sensors,[34,36] light emitting diodes (LEDs),[33,37−40] and microcavity lasers.[41,42] One important feature to add functionality to the nanostructure is having the flexibility of choosing the chemical composition of the product. Chemical synthesis delivers this by allowing elemental, binary, oxide, and heterostructure semiconductors to be synthesized. Although a wide variety of systems can be created, this review will mainly focus on wide band gap semiconductors of ZnO, GaN, and SnO_2, which have been extensively investigated in this lab.

The following serves as a brief outline to the major points discussed in the article. First, it is important to introduce the synthetic techniques, particularly the vapor−solid−liquid (VLS) approach, used to grow arrays of 1D nanostructures. The photoluminescence (PL) properties of individual nanowires will be discussed with special attention to low-temperature excitonic structure, ultrafast carrier dynamics, and polarization anisotropy. After a thorough PL characterization is presented, we discuss nanowire microcavity lasing (ZnO and GaN) and explore the possibility of using these structures as nanoscale coherent light sources. As a compliment to light creation, photodetection with single ZnO nanowire and SnO_2 nanoribbon devices will be

* To whom correspondence should be addressed. E-mail: p_yang@berkeley.edu.

Feature Article

J. Phys. Chem. B, Vol. 109, No. 32, 2005 **15191**

Donald J. Sirbuly received his B.S. degree in chemistry from Westmont College, Santa Barbara, CA, in 1998 and Ph.D. in chemistry from the University of California, Santa Barbara in 2003. Since 2003 he has been a postdoctoral researcher with Professor Peidong Yang at the University of California, Berkeley. His main research interests include the integration of low-dimensional semiconductors into functional device platforms for sensing, photonics and spectroscopy.

Matt Law received B.A. degrees in Chemistry and Government (International Relations) from Wesleyan University in 1999 and is currently a graduate student in Materials Chemistry with Peidong Yang at the University of California, Berkeley, working on nanowire-based photonics and photovoltaics. He was named a 2005 Young Investigator by the Division of Inorganic Chemistry of the American Chemical Society. His research interests are energy conversion and storage, chemical sensing, pollution remediation and the conservation of biodiversity.

analyzed. This naturally leads to the integration of these photoactive elements with passive SnO_2 subwavelength waveguides that can efficiently trap and route photons from nanowire light sources. The passive nature of these waveguides is well described by their ability to shuttle both ultraviolet and visible wavelengths across hundreds of microns. Assembling these nanoribbon waveguides with nanowire lasers and detectors marks the first step toward building nanophotonic circuitry. Finally, we show that nanowire waveguides can efficiently steer and transport light in liquids. The electric field intensity traveling on the outside of the waveguide can be utilized to sense molecules in small liquid volumes (< pL) in proximity to the waveguide surface. This novel property of subwavelength waveguides promises exciting applications in microfluidics and biology.

2. Nanowire Synthesis and Characterization

Single crystalline ZnO nanowires were grown using a simple chemical vapor transport and condensation (CVTC) process described in detail elsewhere.[43,44] The wires were grown on either single crystalline sapphire or silicon substrates using a 20 angstrom gold film as the catalyst. The furnace temperature

Peidong Yang received a B.S. in chemistry from University of Science and Technology of China in 1993 and a Ph.D. in chemistry from Harvard University in 1997. He did postdoctoral research at University of California, Santa Barbara before joining the faculty in the department of Chemistry at the University of California, Berkeley in 1999. He is the recipient of Alfred P. Sloan research fellowship, the Arnold and Mabel Beckman Young Investigator Award, National Science Foundation Young Investigator Award, MRS Young Investigator Award, Julius Springer Prize for Applied Physics, and ACS Pure Chemistry Award. His main research interest is in the area of one dimensional semiconductor nanostructures and their applications in nanophotonics, energy conversion and nanofluidics. More about the Yang group research can be found in http://www.cchem.berkeley.edu/~pdygrp/main.html.

was kept at 900 °C and the growth time ranged from ~5−30 min under a constant flow of argon (20−25 sccm). Wires used in the photoluminescence and lasing experiments had diameters of 100−250 nm and lengths of 3−10 μm. Longer ZnO wires (>20 μm) used as the nanowire light sources in section 7.2 were grown via oxidation of Zn metal on sapphire substrates that were heated to 800 °C in a quartz furnace with 760 Torr of flowing oxygen/argon.[45] Wires were dispersed onto clean substrates by either dry transfer or from methanol/ethanol solutions. Substrates chosen for the transfer varied in their index of refraction and included Si, SiO_x, and sapphire. Unless specified, sapphire was typically used as the support substrate in the photoluminescence and lasing experiments (sections 4 and 5).

Single crystalline GaN nanowires were grown through either a metal-organic chemical vapor deposition (MOCVD)[46] or chemical vapor transport (CVT) process.[47] The MOCVD wires were grown on a variety of different single crystalline substrates including silicon, sapphire, $LiAlO_2$, and MgO. Thin films of metal (Ni, Au, or Fe) were used as the catalyst (thermally evaporated on substrates). Substrates were heated in a quartz tube furnace to temperatures between 800 and 1000 °C for 5−30 min in the presence of flowing trimethylgallium, ammonia, and hydrogen. Total flow rates for the nitrogen and ammonia/H_2 gases were kept constant at 250 and ~155 sccm, respectively. The CVT wires were synthesized on nickel-catalyzed sapphire substrates using a direct reaction with Ga metal and ammonia at 900 °C. Reactions times were varied from 5 min to several hours to produce short (<1 μm) or long (> 200 μm) wires with diameters of 100−200 nm.

Single crystalline SnO_2 nanoribbons were synthesized using a CVT process.[48] SnO powder was placed in a quartz tube furnace and heated to 1100 °C with 350 Torr of flowing argon (50 sccm). The ribbons have rectangular cross-sections with edge sizes of 100−500 nm and lengths of 200−3000 μm. The nanoribbons were collected on an alumina boat and dry transferred to silicon substrates capped with ~1 μm of thermal oxide to perform the optical experiments.

A triple-axis micromanipulator (Märtzhäuser Wetzlär) tipped with an etched tungsten probe (∼400 nm tip diameter) was used to physically manipulate the ZnO, GaN and SnO_2 nanostructures on silica surfaces. To assemble multicomponent networks, individual ZnO and GaN nanowires were removed from their growth substrates and deposited on the same substrate with the SnO_2 ribbons.

Photoluminescence (PL) measurements (from 5 to 300 K) were performed with a continuous wave (CW) unpolarized HeCd laser operating at 325 nm. The excitation was focused onto the sample (single wire or array) with a beam diameter of ∼50 μm at a grazing angle of ∼65° to the direction normal to the substrate. The power density of the laser at the sample was ∼175 W/cm². The sample was placed either on an *x-y-z* translation stage (Figure 1a) or on a dark-field microscope (Figure 1b). The microscope is equipped with a cryostat (Janis ST-500H) for low-temperature single wire or array studies. Emission was collected by a microscope objective (Olympus, NA 0.7 or Nikon, NA 0.55) and imaged by a CCD camera (Photometrics) or routed to an optical fiber coupled to a liquid nitrogen CCD/spectrometer (Roper Scientific). The spectral resolution for the data shown here is 0.1 nm (150 grooves/mm grating) or 0.05 nm (1200 grooves/mm grating). Single wire orientation parameters with respect to the incoming excitation beam and collection optics are shown in Figure 1c. Polarization experiments were carried out by placing either a film polarizer (3M) or polarizing cube into the collection path.

Stimulated emission in the nanowire cavities was generated with UV pulses (310 nm) from the frequency-quadrupled output of an optical parametric amplifier (OPA, TOPAS, Quantronix). The OPA was seeded with regeneratively amplified 800 nm light from a home-built Ti:sapphire oscillator (88 MHz) and commercial regan/bowtie amplifier (1 kHz, 2.5 mJ, Spectra-Physics, Spitfire). The final laser output produced 100−200 fs UV pulses with pulse energies of 2−3 μJ. Neutral density filters were used to control the laser power density. The UV light from the laser was spectrally isolated with a black glass band-pass filter (Edmund, UG11). Where specified, the fourth-harmonic (266 nm) of a Nd:YAG laser (Spectra-Physics, 8 ns pulse width, 10 Hz, 50−100 μJ/pulse) was used to excite the nanowire lasers. The excitation spot from both lasers was focused onto the sample with a CaF_2 or fused silica lens to a spot size of ∼0.02 mm².

Time-resolved second harmonic generation (TRSHG) traces were captured using pulses of near-IR generated from the femtosecond laser described above. Temporal resolution for multiple accumulations was limited to ∼4 ps, whereas single shot data gave a resolution of about ∼1.5 ps. A detailed description of the system is provided elsewhere.[49]

A near-field scanning optical microscope (NSOM) equipped with a chemically etched single-mode optical fiber was utilized for higher spatial resolution spectroscopy (∼100 nm). Details of the experimental setup can be found elsewhere.[50] Simultaneous optical and topographic images (200 × 200 pixels) were obtained with each scan.

Propagation loss measurements were performed on individual SnO_2 nanoribbons dispersed on silica (*n* = 1.45) using the NSOM operating in collection mode. An NSOM probe (an etched single-mode optical fiber) was held fixed over the emission end of single ribbons with lengths greater than 500 microns while the focused UV laser (325 nm) was scanned along their lengths in ∼50 μm increments (approximately the diameter of the beam spot). Propagation losses were calculated after plotting the emission intensity as a function of pump-probe
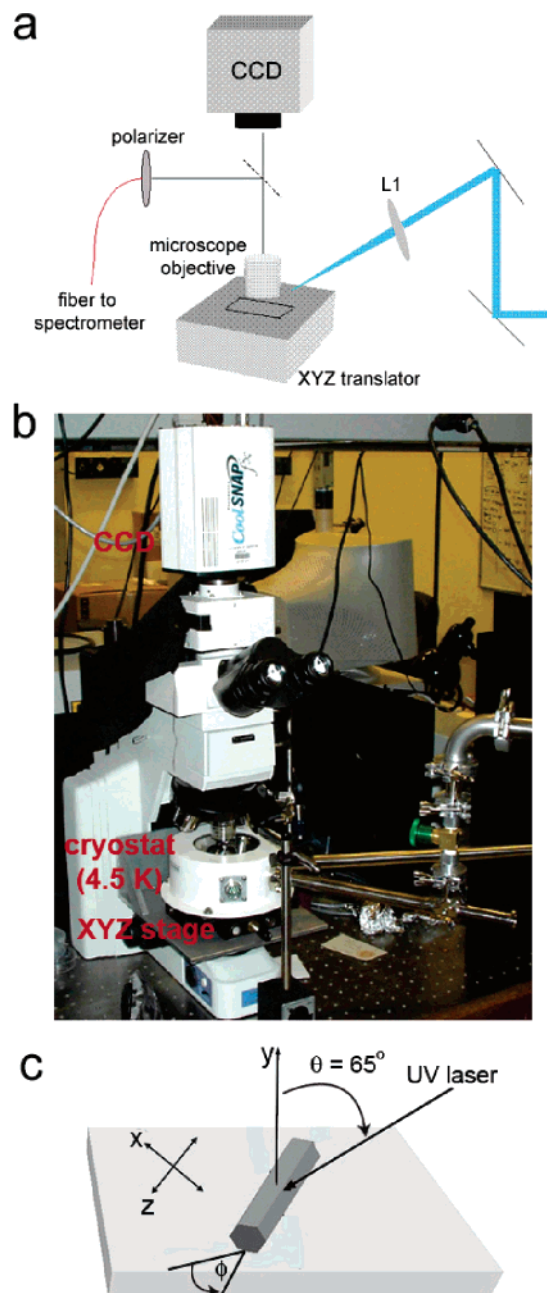
Figure 1. Schematic of the optical setup. (a) Far-field layout of the photoluminescence and stimulated emission experiments. L1 is a 10−30 cm focal length CaF_2 or fused silica focusing lens. (b) Digital picture of the dark-field microscope and integrated 4.5 K cryostat. (c) Magnified view of the nanowire orientation with respect to the laser excitation and substrate. The *z*-direction is along the axis of the wire, while the *x*- and *y*- directions are perpendicular the long axis. The angle ϕ defines the rotation angle of the nanowire in the *x*−*z* plane with respect to the incident plane of the excitation. The angle $\phi = 0$ is defined as the wire axis being orthogonal to the incident plane. The angle θ (generally 65°) describes the azimuthal angle between the pump beam and substrate plane. Reproduced with permission. Copyright 2003 American Chemical Society.

distance. The insertion losses were assumed constant, which is reasonable for the PL generation scheme used in our experiments. Power transfer efficiencies between coupled nanoribbons were determined by comparing the output intensity from one of the ribbon waveguides before and after creating an optical junction between them.

In the liquid experiments, large droplets (∼5 μL) of water or various glycols were transferred to the silica surface with the

Feature Article

J. Phys. Chem. B, Vol. 109, No. 32, 2005 **15193**

ribbons. The smaller volume droplets (as small as 10 fL) were created by dicing the larger droplet and positioning them on the surface using the micromanipulator.

3. Growth of 1D Nanostructures

When growing a 1D single crystal, two fundamental steps emerge which can ultimately influence the quality of the resulting material. The first is nucleation, which involves the initiation of the crystallization process.[51] Whether the solid crystal nucleates from a vapor, melt, or solution, it is crucial to seed the growth with molecules of similar composition to the desired 1D material. The second step is the growth, and in the case of 1D systems it is important to achieve anisotropic growth with good control over size, orientation, and morphology. Of the various vapor phase methods, the vapor−solid−liquid (VLS) mechanism has emerged as an excellent route to controllably produce high quality 1D nanostructures. Wagner and co-workers first used the VLS approach to growing single-crystalline micrometer-sized whiskers in the 1960s.[52] In recent years, it has found its way back to the synthetic table to grow a variety of inorganic 1D nanostructures.[44,53−75]

In VLS growth, a metal catalyst particle resting on a solid surface serves as a dissolution medium for incoming gaseous species at elevated temperatures. As the metal alloy becomes saturated with the precursor molecules, a precipitation event occurs that forms the base of the nanowire. The growth persists under a continual dissolution−crystallization cycle and is guided along a single dimension by the interfacial energy between the crystal and metal droplet. It is important to choose a metal catalyst with proper thermal stability and solubility for the gaseous precursors. Additional information on VLS growth and other vapor and solution phase growth mechanisms for 1D nanostructures can be found in recent reviews by Xia et al.[30] and Law et al.[76]

In an attempt to capitalize on the synthetic control that the VLS approach offers, efforts have been directed to controlling the growth direction of promising optoelectronic materials such as GaN and ZnO. The VLS process has been shown to give excellent control over nanowire location and size (i.e., wire diameter and length).[77−82] However, the ability to choose the crystallographic growth direction of a nanowire array would aid in tuning the physical properties of the material, including spontaneous piezoelectric polarization, thermal and electric conductivity, dielectric constant, lattice strain, and band gap. Recently, we demonstrated such control of the crystallographic growth direction of wurzite gallium nitride nanowire arrays.[83] Using metal-organic chemical vapor deposition (MOCVD), vertically aligned nanowire arrays grown on (100) γ-LiAlO$_2$ and (111) MgO single crystalline substrates resulted in wires oriented along the [110] and [001] growth axes, respectively. These orthogonal crystal directions produce nanowires with triangular or hexagonal cross-sections that have markedly different emission properties. This approach shows great promise both for the compatibility of the gas-phase synthesis with thin film technology and for tuning the optical properties of 1D inorganic semiconductors based on lattice strain or piezoelectric effects.

Scanning electron micrographs (SEM) of the [110] and [001] oriented GaN arrays are shown in Figure 2. The triangles (Figure 2a) are actually isosceles in nature due to the 2-fold symmetry match of wurzite GaN with the oxygen sublattice of the (100) plane in γ-LiAlO$_2$. Likewise, the hexagonal shape (Figure 2b) arises from the 3-fold symmetry registry between the GaN and the (111) plane of MgO. Further characterization is shown in
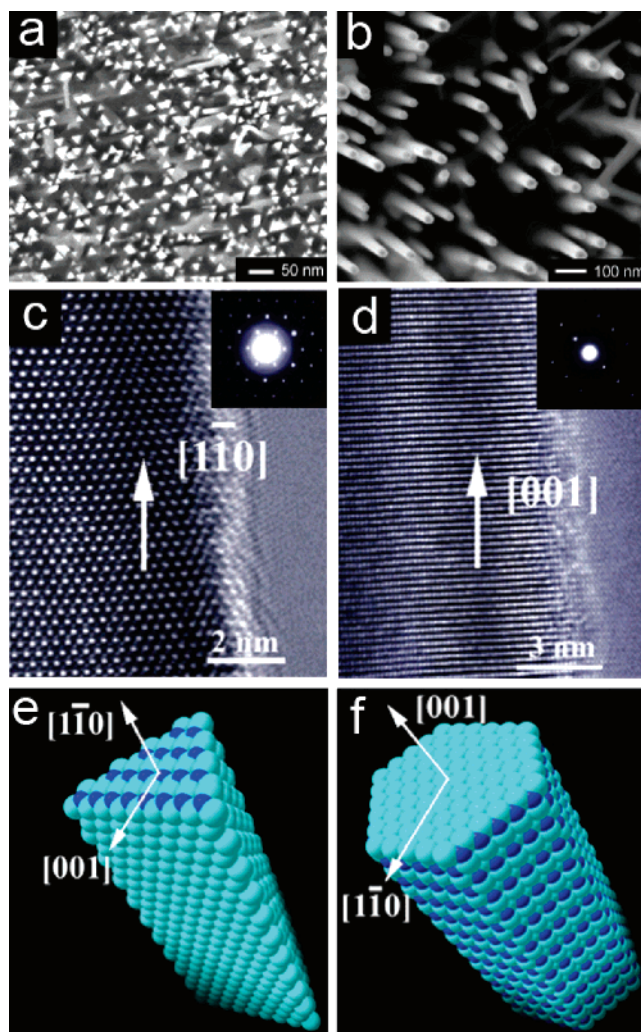

Figure 2. Scanning and transmission electron micrographs of the aligned GaN nanowires. (a) SEM and (c) TEM of [110] oriented wires grown on (100) γ-LiAlO$_2$, respectively. Inset in (c): Electron diffraction pattern recorded along the [001] zone axis. (b) SEM and (d) TEM of [001] oriented wires grown on (111) MgO. Inset in (d): Electron diffraction pattern recorded along the [110] zone axis. (e,f) Space-filling structural models for the [110] and [001] oriented wires, respectively. Reproduced with permission. Copyright 2004 Nature Publishing Group.

the transmission electron micrographs (TEM) in Figure 2c,d. From the electron micrographs it is apparent that the wires grown on (100) γ-LiAlO$_2$ and (111) MgO substrate have orthogonal growth axes, and that they can be grown with cross-sectional dimensions ranging from 15 to 40 nm with lengths greater than 10 μm. A similar approach can be used to gain orientation control in ZnO nanostructures. Hexagonal ZnO wires are well-known,[42,84] but when grown on LiAlO$_2$ the ZnO wires grow along the [110] direction and have rectangular cross-sections.

4. Photoluminescence Properties

Optical spectroscopy of semiconductor crystals can provide useful information on carrier dynamics (e.g., radiative lifetimes, nonradiative trapping), carrier confinement, collisional effects (i.e., Auger recombination) and other properties. As the dimensions of a bulk semiconductor are reduced to the nanometer regime, many of these phenomena, which typically occur at relatively short time scales, can be either enhanced or quenched. Furthermore, collisional effects begin to compete with radiative
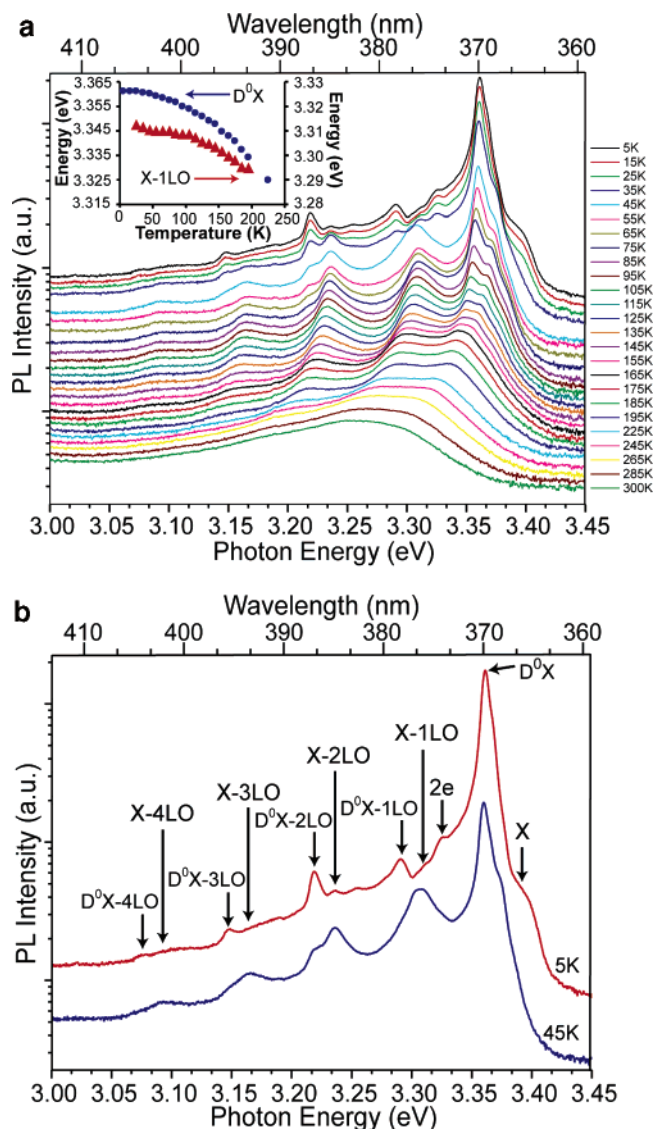
Figure 3. Low-temperature series on a single ZnO nanowire. (a) Log plot of the band edge emission as a function of temperature (pump power ~50 W/cm²). The inset plots the donor bound (D⁰X) and first-order free-exciton phonon replica (X-1LO) peaks as a function of temperature. (b) Zoom in of the 5 and 45 K spectra showing the excitonic fine structure. Note the transition between the donor bound and free exciton domination occurs at ~45 K.

mechanisms and can obscure nonradiative decay processes in small crystallites, especially at high carrier densities.

4.1. Low-Temperature Photoluminescence. A convenient technique to discern the optical quality of a semiconductor is to freeze out thermal processes that contribute to line shape broadening, nonradiative recombination, defect population, etc., and directly probe the electronic states of the material. Low-temperature PL spectroscopy on single nanostructures offers high spectral resolution and eliminates ensemble averaging due to inhomogeneity in the nanowire arrays. It is straightforward to study isolated nanowires, nanotubes, and nanoribbons as a function of temperature using our integrated cryostat/dark-field microscope system. Since ZnO nanowires are one of the promising optoelectronic materials for future nanophotonic devices, they provide a model system for studying the effect of temperature on excitonic species.

ZnO is a popular optoelectronic material because of its strong ultraviolet emission (band gap of ~3.37 eV at room temperature) and large exciton binding energy (~60 meV). Figure 3a shows
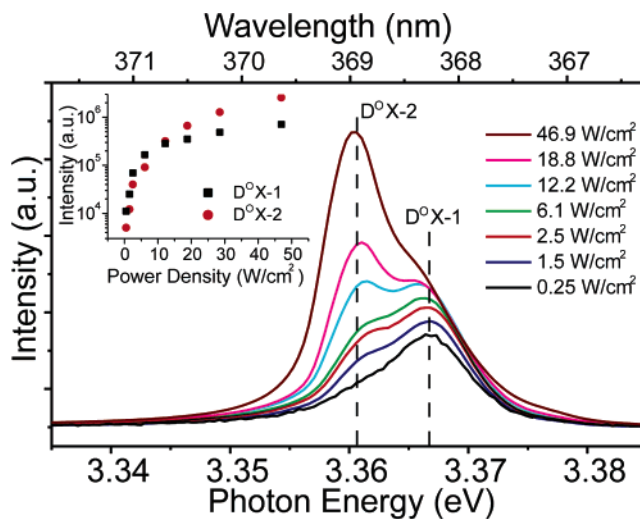

Figure 4. Power dependent photoluminescence of a single ZnO nanowire at 5 K. Tuning two donor bound transitions as a function of power. The D⁰X-2 is generally the strongest peak once higher (>10 W/cm²) power densities are attained. Inset: Plot of the fitted emission intensity for the D⁰X-1 and D⁰X-2 transitions as a function of power density.

the temperature-dependent PL of a single ZnO nanowire. The spectra are plotted on a logarithmic scale from 5 to 300 K. The low temperature (<45 K) spectra (Figure 5b) are dominated by a neutral-donor bound exciton (D° X-2) centered at 3.361 eV and four donor bound phonon replicas (LO) located at 3.291 eV (D° X-1LO), 3.218 eV (D° X-2LO), 3.147 eV (D° X-3LO), and 3.0772 eV (D° X-4LO). The D° X-2 transition agrees well with previously assigned donor-bound excitons in single crystals,[85] epilayers,[86,87] and nanorods.[88] The average energy spacing between donor bound LO replicas is 71.2 meV, in good agreement with values of ~72 meV reported for ZnO films and quantum well structures.[89,90] This LO spacing predicts a donor bound peak at 3.362 eV, compared to the experimentally determined value of 3.361 eV.

The low-temperature spectra also provide evidence for the free exciton (X) transition located at 3.386 eV, as well as two of its phonon replicas, denoted X-1LO and X-2LO, at 3.312 and 3.236 eV, respectively. The free exciton peak, with a full width at half-maximum (fwhm) of ~38 meV, is a combination of both free A and B excitons,[91] arising from anisotropic transitions between the p-like valance bands and s-like conduction band.[92,93] The peak centered at 3.326 eV is assigned to a two electron (2e) transition that commonly accompanies a neutral-donor bound transition.[86,94] The higher third and fourth order free exciton phonon replicas (X-3LO and X-4LO) at 3.167 and 3.094 eV, do not emerge from the emission profile until ~45 K (Figure 4b). At this temperature, the free excitonic phonon replicas begin to dominate the donor bound phonon transitions due to thermal quenching of the donor bound excitons. The average energy splitting between the higher order X-LO transitions of 72.1 meV is in good agreement with the calculated splitting of the donor bound LO peaks and provides additional support that these peaks arise from lattice-assisted radiative transitions. Furthermore, the free exciton (X) peak can be estimated to occur at 3.384 eV using the LO splitting, which is within 2 meV of the experimental value of 3.386 eV. The band gap energy versus temperature for the D° X-2 and X-1LO transitions are plotted in the inset of Figure 3a. By fitting this curve to a Varshni expression,[95] $E_g(T) = E_g(T_0) - \alpha T^2 (\beta + T)^{-1}$ (where $E_g(T_0)$ is the band gap energy at 0 K, T is the temperature, and α and β are fitting parameters), we

Feature Article

J. Phys. Chem. B, Vol. 109, No. 32, 2005 **15195**
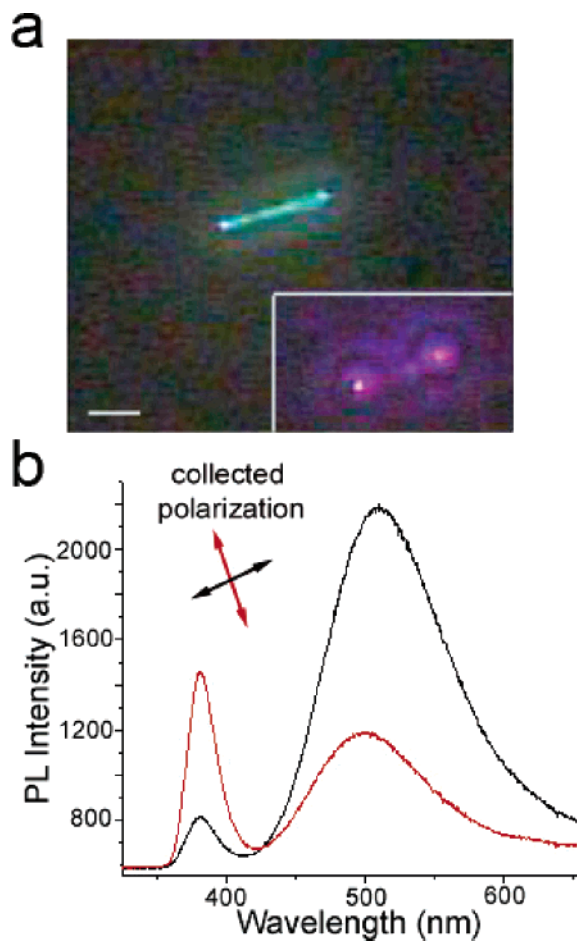
Figure 5. Spontaneous emission polarization dependence of a single ZnO nanowire. (a) Far-field PL image and (b) PL spectra of a wire excited with unpolarized 325 nm light ($\phi = 0°$). The emission was collected with a polarizer aligned either along the major axis (black curve) or perpendicular to it (red curve). The inset in (a) shows a stimulated emission image of the waveguided band edge emission under pulsed excitation. Scale bar = 5 μm. Reproduced with permission. Copyright 2003 American Chemical Society.

found $\alpha = 1.3$ meV/K and $\beta = 970$ K. The data points in the temperature series do not extend pass $\sim$250 K due to difficult assignment of the two peaks once they merge at elevated temperatures.

At low temperature is also possible to tune the neutral-donor bound excitons by altering the excitation power density. This can be done either by translating the wire across the Gaussian excitation beam or by attenuating the laser power. Figure 4 illustrates that at low power densities ($<$10 W/cm^2) the emission profile is dominated by a higher energy donor bound peak (D° X-1) at 3.367 eV. At power densities above 10 W/cm^2, a lower energy peak (D° X-2) at 3.361 eV is promoted. The inset in Figure 4 plots the logarithmic intensity of both peaks versus the power density. A majority of the donor-bound transitions tuned in this way have most of their emission intensity ($>$ 99%) centered on the D° X-2 at higher powers ($>$ 10 W/cm^2). The exact nature of these bound excitons is not known at this time. Thermal variations caused by nonradiative processes are assumed to be negligible under these conditions. Further low-temperature studies, including an investigation of nanowire photoconductivity and carrier lifetimes, will be necessary to determine the origin of these excitonic features.

4.2. Spontaneous Emission Polarization. Room-temperature ZnO nanowire PL is characterized by a narrow band-edge emission peak at 385 nm (fwhm $\sim$15 nm) and a defect emission

band at 510 nm (fwhm $\sim$100 nm). The near-UV PL arises from free- and donor bound exciton recombination, while the green defect PL is believed to be caused by paramagnetic oxygen vacancies[96−98] and/or Zn interstitials. The PL of a single nanowire has strong polarization anisotropy, as shown in Figure 5 for a single wire (supported on sapphire) oriented at $\phi = 0°$. The z-polarization (ρ_z), defined as $\rho_z = (I_z - I_x)/(I_z + I_x)$, for the UV emission is strongly negative ($\rho_z = -0.65$) along the x-direction, whereas green emission is preferred along the z-direction ($\rho_z = 0.55$). A similar polarization is observed when the wire is rotated to $\phi = 90°$.

It can be concluded that the variations in polarization for band edge and defect emission results from different dipole orientations in their emission. One would expect strong coupling of PL to guided cavity modes if the emission is strongly waveguided along the wire axis, as is the case for the UV PL (Figure 5a, inset). The guided UV would be partially polarized along the x and y directions but detected as isotropic due to the collection geometry being sensitive to only the x and z components. Therefore, a negative value in the polarization likely signifies an enhanced coupling of the waveguided emission to the substrate. Alternatively, a positive polarization indicates a well-defined dipole along the axis of the nanowire and a weak coupling to waveguided modes. Since the efficiency of PL coupling to axially guided modes varies inversely with the wavelength of light, one would expect a strong axial radiation dipole due to the reduction of modal power within the core at longer wavelengths. Assuming a cylindrical waveguide of radius r, the fractional mode power confined within the core can be estimated by[99]

$$\eta = 1 - (2.405e^{-1/V})^2 V^{-3} \qquad (1)$$

where $V = kr(n^2-1)^{1/2}$ (r is the wire radius, n is its refractive index, and $k = 2\pi/\lambda$). Wires with $r > 100$ nm will have $>$90% of the field intensity (lowest order guided mode) within the core ($\lambda = 380$ nm). However, when $r = 50$ nm, $<$25% of the field intensity is carried within the nanowire. The percentage of field intensity outside of a given nanowire cavity will be higher for the longer wavelength defect emission as compared to the band-edge emission, making it more susceptible to diffraction effects. This topic of photonic confinement becomes more important when optical gain in the nanowire microcavities must be maximized for efficient lasing (discussed in section 5). If the nanowire is treated as an infinitely long dielectric cylinder, a polarization ratio of 0.85 for the green emission would be expected since the x-polarization component would steadily decrease by $2\epsilon_0/(\epsilon+\epsilon_0)$, where ϵ_0 and ϵ are the dielectric constants of vacuum and ZnO, respectively. Experimentally, the polarization ratio reaches $\sim$0.75 for the longest wires studied (about 22 μm). The predicted polarization of 0.85 is only an upper limit for the experimental values. The increase in polarization is nearly linear, but can be heavily influenced by nanowire shape and structural variations as well as substrate coupling.

4.3. Ultrafast Carrier Dynamics. To better understand the carrier dynamics immediately following an absorption event, it is imperative to study both the radiative and nonradiative decay processes as a function of carrier concentration. Transient PL spectroscopy offers a method to study the radiative relaxation dynamics but is not a good probe of nonradiative events such as surface-localized trapping, carrier scattering, or Auger recombination[100] that are known to be enhanced in nanoscale materials.[101] Time-resolved second harmonic generation (TRSHG), on the other hand, probes the ground-state dynamics

of a system and is sensitive to the sum of its radiative and nonradiative recombination rates. The complementary use of these two techniques provides a more complete picture of the excitation and relaxation processes occurring in semiconductor nanowires.

ZnO nanowires (diameters < 175 nm; lengths > 5 μm) are known to have lasing thresholds (P_{th}) as low as ~70 nJ/cm^2 under femtosecond optical excitation.[102,103] Most studies support an exciton−exciton (EE) recombination mechanism (discussed in more detail in section 5.1) as the primary lasing mechanism under low pump intensities (near the lasing threshold). An electron−hole plasma (EHP) mechanism dominates lasing under high pump fluences. Previous time-resolved experiments on disordered ZnO thin films showed a fast decay (several ps) that correlated well with the observed stimulated emission.[104−107] However, details of the underlying lasing mechanism remains unclear.[49]

Transient PL studies (ps time resolution) are relatively straightforward.[108,109] Earlier transient PL experiments on bulk ZnO crystals revealed a biexponential decay process consisting of a fast 70−100 ps component (τ_1) and a slow decay (τ_2) of 400−600 ps.[110,111] The fast decay component (τ_1) in the bulk is similar to what is observed in the individual ZnO nanowires (75−100 ps) when the pump fluence is kept below the lasing threshold (Figure 6). The slow decay time is not readily seen under these excitation conditions, as the signal is too weak to detect. Once the power density is increased above the lasing threshold, as determined by the power trace and stimulated emission spectra (Figure 6b), a fast decay component (~10 ps) rapidly emerges that is nearly an order of magnitude faster than what is observed in the bulk. Furthermore, this fast decay constant continues to decrease nearly to the resolution of the instrument (~4 ps) as the pump intensity approaches saturation. A reasonable explanation for the large discrepancy between the fast (10 ps) and slow (75−100 ps) time constants is that the high density of excited states (under EHP), created in a short amount of time (<100 fs), causes a rapid annihilation of the carriers. This cascade of excitons is responsible for providing the necessary optical energy to support gain and lasing in the nanowire cavity. Although difficult to quantify due to detector limitations, the fast decay amplitude (as a function of pump power) does display a nonlinear response. This response is similar to what is observed in a single nanowire power curve (see section 5.1). Under exciton−exciton or EHP, the depletion of the excited state should be well described by a bimolecular expression $1/N = 1/N_0 + Bt$, where B is the effective bimolecular rate constant, N is the population of excited states after excitation, N_0 is the maximum population attained, and t is the time delay after pumping. The fast decay fits well to a bimolecular decay. However, it is difficult to exclude other models since a low signal-to-noise ratio could be screening contributions from other relaxation pathways.

To gain more information on the excited-state and ground-state dynamics, while reducing the background noise inherent to transient PL, time-resolved second harmonic generation (TRSHG) can be performed.[49] Since noncentrosymmetric materials show a lowest order nonlinear susceptibility ($\chi^{(2)}$) that is reasonably high, they can generate a fairly high SHG signal.[112] Previously it was shown that an increase in excited states in a highly noncentrosymmetric material causes a decrease in ($\chi^{(2)}$) and a lower SHG signal.[113] The recovery in ($\chi^{(2)}$), therefore, is a combination of both radiative and nonradiative relaxation; providing additional information on the excited-state and ground transient properties. At pump powers below the lasing threshold,
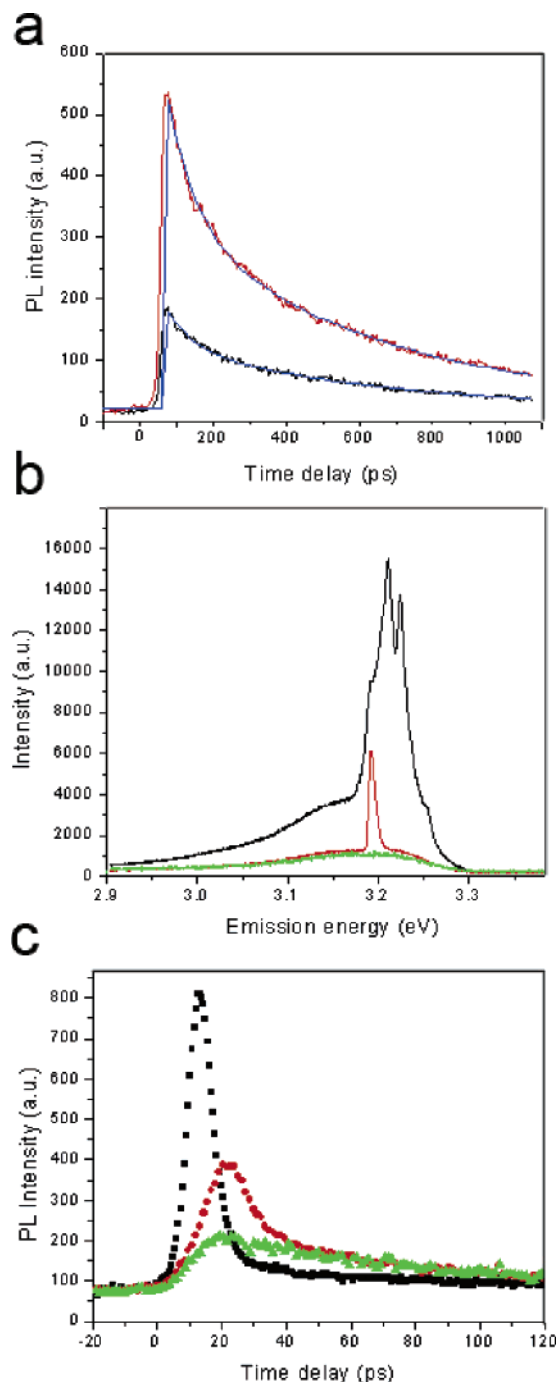
Figure 6. (a) Transient decay response of the bulk PL in a single ZnO nanowire at low (<5 μJ/cm^2, black curve) and high (>20 μJ/cm^2, red curve) pump powers. The biexponential fits (blue curves) gave time constants of $\tau_1 = 75 \pm 10$ ps and $\tau_2 = 550 \pm 50$ ps. (b) Photoluminescence and stimulated emission spectra at pump powers near P_{th} (~1 μJ/cm^2). (c) The transient PL response for the series shown in (b). The long decay (green curve) component is 70 ± 7 ps and the short components at higher pump powers are 9 ± 0.8 ps (red curve) and 4.0 ± 0.3 ps (black curve). Reproduced with permission. Copyright 2004 American Chemical Society.

the transient SHG signal displays a weak single-component decay with a time constant of ~50 ps. As the pump power is increased above the lasing threshold, the decay constant shortens to <25 ps. A fast component also emerges as the pump fluence is increased from the lasing threshold to saturation. Similar to the transient PL dynamics, this short time constant decreases from ~5 ps (just above the lasing threshold) to near 1 ps as the carrier concentration saturates at high pump power. The nearly

Feature Article

*J. Phys. Chem. B, Vol. 109, No. 32, 2005* **15197**

identical trend between the TRSHG and transient PL short time constants suggest that a similar stimulated emission effect, such as multibody collision, is responsible for carrier recombination. Unlike the transient PL, however, the long decay component in the transient SHG experiments does depend on the pump fluence. This can be interpreted as a nonradiative contribution to the slow decay component and suggests that scattering events are involved. It should be noted that the fast component, which is attributed to stimulated emission, was not observed in structures that showed no lasing behavior.

5. Nanowire Microcavity Lasers

A major hurdle for miniaturizing photonic devices is to produce reliable coherent light sources that offer strong, directional emission. The recent discovery of room-temperature lasing in semiconductor nanowires of ZnO,[41,103] GaN,[47] and CdS[42] has spurred much interest in studying the fundamental properties of these lasers and integrating them into optoelectronic devices. These structures act as waveguides for specific axially guided modes and provide sufficient resonant feedback for low gain threshold values and high quality factors.

The remarkable photonic confinement in nanoscale cavities is mainly due to the high refractive index difference between the semiconductor material and its surrounding dielectric environment. This strong optical confinement aids in achieving mode gain by supporting guided modes and providing an excellent resonant cavity for light amplification. Classical optical waveguide theory can be used to understand the effects of electromagnetic fields as modes propagate through the cavity; however, it remains a challenge to elucidate the exact lasing mechanism in these structures, due mostly to variations in modal gain (i.e., mode reflectivity differences). For theoretical modeling, the cavity is assumed to be a perfect vertical cylinder surrounded by an air cladding, which makes the extraction of reflectivity,[114] far-field emission patterns,[115] and modal gain[116] of the lowest-order bound modes possible. Experimentally, however, the nanowire lasers are typically studied in a horizontal configuration. This geometry makes it difficult to quantify the effect of the substrate on losses, bound modes, and surface reflectivities. In any case, recent theoretical work on electromagnetic effects in these cavities provides substantial insight into the experimental studies on the lasing properties of these materials.

5.1. Cavity Mode Gain and Lasing Thresholds. Room temperature stimulated emission was originally observed in ZnO bulk thin films in 1997,[117] and later in dense particle networks in 1998.[118] Lasing in 1D nanostructures was observed a few years later in 2001.[41] From the thin film research, it has been proposed that the onset of lasing is induced by exciton−exciton (EE) collisions that stimulate recombination events.[119,120] The EE mechanism was briefly mentioned in section 4.3 to exist due to the large room temperature binding energy of ZnO (60 meV). This sort of recombination is prevalent in the nanowire at low pump power, but it does not fully explain the strong gain observed at high carrier concentrations. As the electron and hole concentrations increase, there is a direct consequence of the higher carrier numbers on the Coulombic interactions between the charge carriers. The binding energy decreases as the number of excitons increase due to screening caused by the strong Coulombic forces between the excitons and free carriers. This interaction produces a destabilized exciton when the Bohr radius equals the critical screening length and leads to an electron−hole plasma (EHP) state at elevated pump intensi-
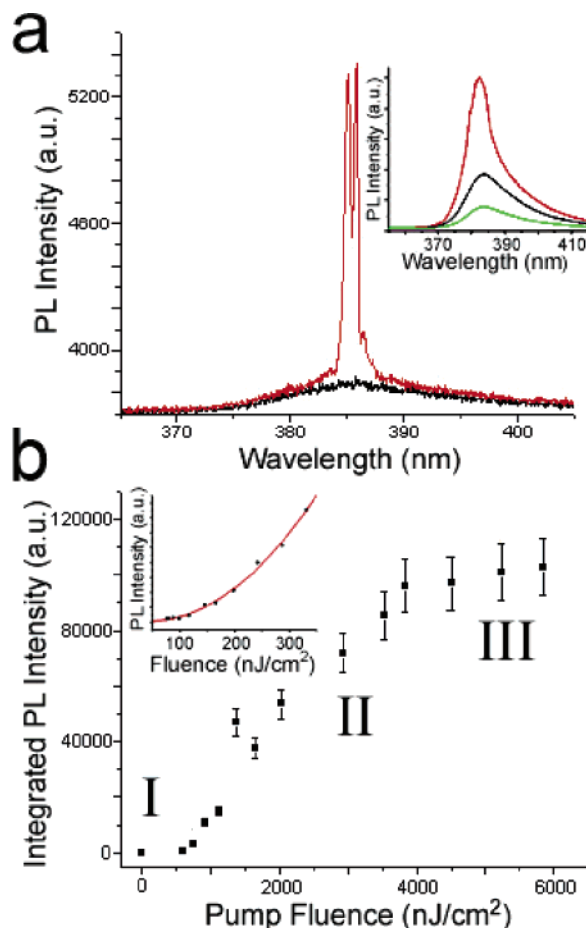
Figure 7. Lasing in individual ZnO nanowires under femtosecond excitation. (a) Spectra recorded at 300 nJ/cm² (black) and 450 nJ/cm² (red), illustrating the sharp transition from spontaneous to stimulated emission. Inset: Spectra recorded at 200 nJ/cm², 350 nJ/cm², and 2000 nJ/cm² showing ASE in a larger diameter wire. (b) Overall power dependence curve, showing the various excitation regimes including spontaneous emission (region I), stimulated emission (region II), and saturation (region III). Inset: Magnified view of region I (80 nJ/cm²) showing the P^2 power dependence of the emission (P_{th} = 80 nJ/cm²). The red curve is a quadratic best fit. Reproduced with permission. Copyright 2003 American Chemical Society.

ties.[121] In a bulk ZnO crystal, the transition from an EE to EHP state should take place when the carrier density exceeds the Mott density (n_m) which is proportional to $1.19^2 k_b T \epsilon \epsilon_0 (ea_b)^{-2}$, where e is the charge of an electron, a_b is the Bohr radius, ϵ is the dielectric constant of ZnO, and T is temperature. For bulk ZnO the Mott density is approximately 4×10^{18} cm⁻³. In other materials such as GaN, a similar EHP mechanism is likely responsible for lasing; however, the amount of gain experienced under this process is thought to be lower due to a smaller exciton binding energy (~26 meV) and more efficient excitonic recombination.[122]

A transition from spontaneous to stimulated emission is generally marked by a narrowing in the emission line shape as bound modes start to experience gain. It is common to see line shapes narrow to sharp modes with full width half-maxima (fwhm) approximately 1/100 of the spontaneous emission. A representative transition from spontaneous to stimulated emission in a single ZnO nanowire laser is observed in Figure 7a. In larger wires this transition occurs much more smoothly (Figure 7a, inset), and does not show the sharp narrowing in the mode structure. This behavior is similar to the line narrowing expected for amplified spontaneous emission (ASE). Here one

can estimate the line width by[123]

$$\Delta\nu_{ASE} = \Delta\nu_0[(G-1)/G\ln G]^{1/2} \qquad (2)$$

where $\Delta\nu_0$ is the initial spontaneous line shape and G is the gain. If gain values that are equivalent to twice the lasing threshold intensity are used, a line width of 0.62 is found.

Under a steady-state condition (wire geometry and pump conditions are fixed), the electric field inside the nanowire is a superposition of forward- and back-reflected guided modes. Analogous to a macroscopic Fabry−Perot (FP) resonator, the nanowire cavities should support longitudinal modes (traveling along the wire axis) with a spacing ($\Delta\nu_c$) equal to $c/2nL$, where L is cavity length and n is the refractive index. This mode spacing is based on a simplified treatment of a cavity that satisfies a standing wave condition and neglects any dispersion effects. By including the dispersion properties, the mode spacing can be expressed as[124]

$$\Delta\lambda = \frac{\lambda^2}{2L\left(n - \lambda\dfrac{dn}{d\lambda}\right)} \qquad (3)$$

where L is the length of the cavity, λ is the mode wavelength, n is the index of refraction at λ, and $dn/d\lambda$ is the first-order dispersion relation ($\lambda\, dn/d\lambda \cong -1.0$ for ZnO) at λ.[125] For the typical nanowire laser with a $L \sim 10\ \mu$m and $n = 2.4$, the mode spacing is approximately 2 nm, which is in good agreement with the experiment (see Figure 7 and Figure 8).

The number of bound transverse (M_{bm}) modes can be modeled assuming a cylindrical optical cavity. Here M_{bm} is approximated by[99]

$$M_{bm} = 2(\pi r/\lambda)^2(n^2 - 1) \qquad (4)$$

where r is the radius, λ is wavelength, and n is the refractive index of the cavity. For wires with radii between 50 and 300 nm, the number of bound transverse modes is between 1 and 6 ($\lambda = 380$ nm). The single-mode cutoff diameter of a cylindrical cavity depends on the waveguide parameter V:

$$V = \frac{\pi d}{\lambda}(n_{co}^2 - n_{cl}^2)^{1/2} \qquad (5)$$

where d is the diameter, λ is the free-space wavelength of light ($V = 2.405$ for single mode operation), and n_{co} and n_{cl} are the refractive indices of the core and cladding, respectively. For a ZnO nanowire the single-mode cutoff diameter is $\sim$130 nm at 380 nm.

The transition from spontaneous to stimulated emission in wires with smaller dimensions (thickness and length) is predicted to be subtle. Experimentally it is difficult to capture lasing in such small cavities due to the large gain ($> 10^4$ cm^{-1}) necessary to overcome losses caused by the poor end facet reflectivities of the nanowire. If one neglects external losses imposed by the substrate or background, the threshold gain for a Fabry−Perot resonator can be calculated according to:[126]

$$G_{th} = (2L)^{-1}\ln(R^2)^{-1} \qquad (6)$$

where R is the end facet reflectivity ($\sim$0.20 for ZnO/air). The predicted gain threshold coefficients for a single ZnO or GaN nanowire the G_{th} is calculated to be between 400 and 3000 cm^{-1}. These values are somewhat comparable to bulk thin films ($\sim$180−2000 cm^{-1}),[107,127,128] likely due to the strong photonic
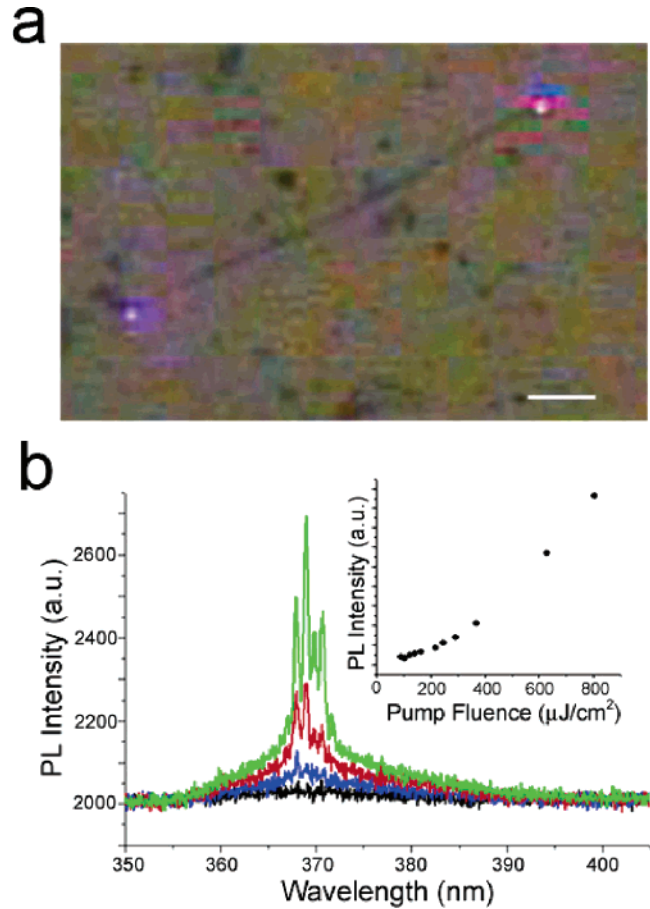
Figure 8. Power dependence of a single GaN nanowire. (a) Far-field PL/bright-field image of a GaN nanowire pumped above the lasing threshold showing strong waveguiding of the UV emission to the ends of the wire. Scale bar = 5 μm. (b) Power dependence spectra of a GaN nanowire under nanosecond excitation. Spectra taken at 142, 218, 292, and 368 μJ/cm^2 Inset: Power curve of the same wire ($P_{th} \sim$ 150 μJ/cm^2).

confinement in the nanoscale cavities allowing the gain to overcome cavity losses.

From a theoretical standpoint, gain values can be extracted by first identifying the bound modes of the cavity. The predominant modes that exist within nanowires with radii $\sim$100 nm are the fundamental (HE$_{11}$) and two transverse modes TE$_{01}$ and TM$_{01}$. Each of these modes has unique polarization components associated with them, leading to various far-field diffraction patterns,[115] end facet reflectivities,[114] and modal gain coefficients.[116] One would expect the TE$_{01}$, which has only a transverse electric field component, to experience gain along the transverse direction. The HE$_{11}$ and TM$_{01}$ modes, on the other hand, have both longitudinal and transverse components and would experience gain along both directions. Maslov et al. have performed optical gain calculations on the guided HE and TE/TM modes in nanowire lasers by first calculating the mode confinement factors and using them in conjunction with the gain derived from bulk crystals to extract the modal gain.[116] For a fixed carrier density of $N = 2 \times 10^{19}$ cm^{-3}, radius of 75 nm, and temperature $T = 300$ K, the TM$_{01}$ experienced a maximum modal gain values of less than 300 cm^{-1}, whereas the HE$_{11}$ and TE$_{01}$ modes underwent modal gains of slightly greater than 1750 and 2000 cm^{-1}, respectively. Although performed on a simplified nanowire geometry (free-standing in air), these gain calculations provide convincing evidence that the HE$_{11}$ and TE$_{01}$ are the predominant modes responsible for lasing in nanowire cavities with radii < 100 nm.

Feature Article

*J. Phys. Chem. B, Vol. 109, No. 32, 2005* **15199**
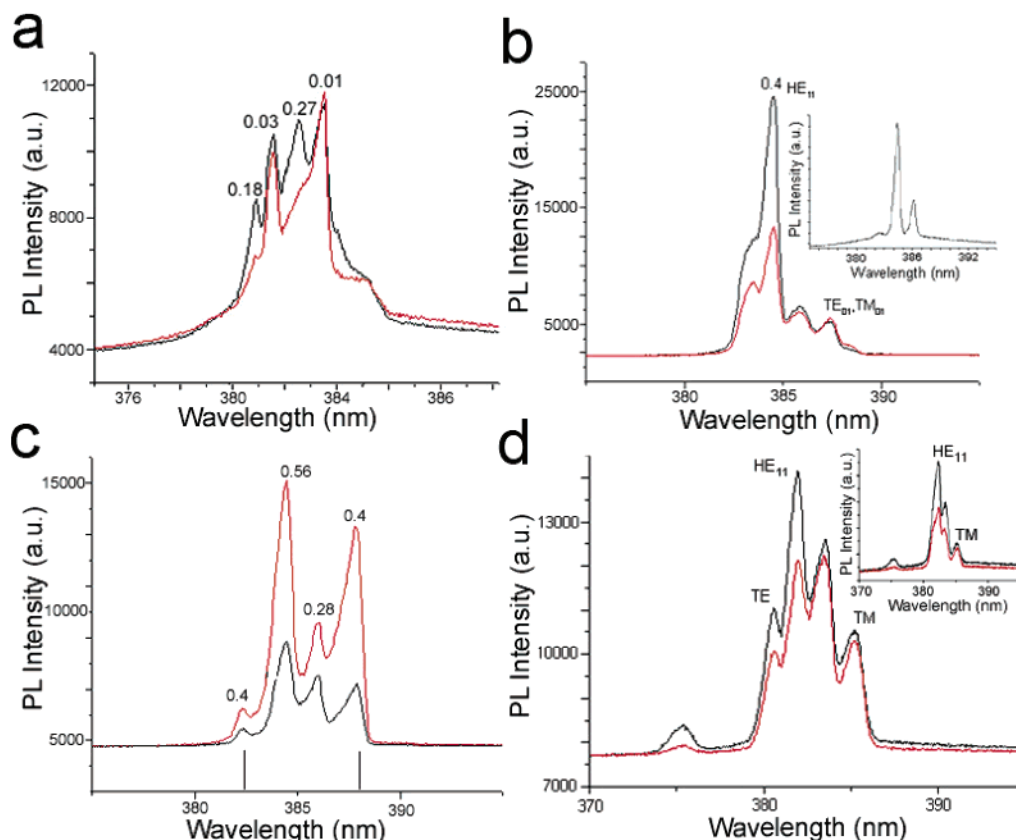
Figure 9. Polarization dependence of individual laser modes for a single ZnO nanowire. (a) Stimulated emission spectra collected with a polarizer aligned along the x- (black) or y-direction (red). The polarization memory (ρ_x) for each mode is given. (b,c) Spectra collecting the x- (black) and y-polarized (red) emission on a wire oriented at $\phi = 0°$ and $\phi = 90°$, respectively. The collection polarizer was oriented in the same direction in both (b) ($x -$ red) and (c) ($x -$ black). Inset in (b): Spectrum collected near the lasing threshold showing the lowest threshold modes. (d) Spectra recorded on a nanowire oriented orthogonal to the incident plane with the incident beam polarized in the plane of incidence. Inset: Spectra recorded on the nanowire oriented orthogonal to the incident plane with the incident beam polarized parallel to the substrate plane. The black traces were obtained with the collection polarizer aligned to pass x-polarized light. Reproduced with permission. Copyright 2003 American Chemical Society.

Although difficult to compare the theoretical predictions on modal gain, experimental power curves can be performed on individual wires to capture the overall lasing response as a function of pump power. These data sets contain information on the gain experienced in individual modes, but it is arduous to deconvolute the gain from cavity shape effects, gain profile shifts, and substrate coupling. Figure 7b plots a typical power curve for an individual ZnO nanowire. The lasing threshold of this particular nanowire is ~80 nJ/cm² and illustrates the nearly linear and quadratic dependence of the emission below and above P_{th}, respectively. A saturation of the lasing intensity can also be observed if the pump fluence is increased beyond ~5 μJ/cm². To extract an estimated carrier density at various pump intensities, one can assume that all photons striking the nanowire (310 nm excitation) are absorbed. This is a good assumption because of the high absorption coefficient (> 10⁵ cm⁻¹) of ZnO and the relatively short penetration (~100 nm) depth compared to the wire's diameter (~120 nm). The carrier densities, at lasing threshold and at saturation, are calculated to be 2×10^{17} and 5×10^{18} cm⁻³, respectively. The carrier density at saturation, obtained at pump fluences of ~3−5 μJ/cm², is actually very close to the Mott density of ZnO (4×10^{18} cm⁻³), which suggests that an EHP type lasing mechanism is operative. However, the gain curve does not continue to increase, but instead saturates, thus making a simple assignment of the transition from EE to EHP nontrivial. A closer look at the power curves shows a nearly linear response in emission intensity at pump powers below P_{th} (region I). The transition to lasing is generally a quadratic (Figure 7b, inset) dependence on the pump

power (region II), but in some cases the response is linear. The gain saturation occurring at high pump fluences (region III), however, does not abide by a simple gain analysis. Thermal population of the lower lying lasing states is a likely explanation for the onset of saturation. Here the increasing carrier density in the lower energetic states causes the degree of population inversion to be pinned. Further experimentation, however, should provide a better understanding of the EHP dynamics occurring in the nanowires.

In GaN, similar power dynamics are observed. The data shown in Figure 8 are representative of a single GaN nanowire laser under nanosecond excitation. Figure 8a is a PL/bright-field image of lasing nanowire (length ~40 μm, diameter ~300 nm) supported on sapphire. The line shape variation between spontaneous (black curve) and stimulated emission (green curve) can be seen in the power spectra (Figure 8b). The spontaneous emission is broad and featureless and the stimulated emission spectra show several emerging sharp peaks (fwhm < 1 nm), corresponding to longitudinal Fabry−Perot cavity modes. As discussed earlier, the weaker excitonic binding energy in GaN (~26 meV) and increased Coulomb screening at high carrier concentrations causes the predominant lasing mechanism to be EHP.[122] Under nanosecond excitation, we typically observe a 2−3 orders of magnitude increase in the P_{th} (Figure 8b, inset) when pumping with a laser ~100 times longer than the radiative lifetime (> 100 ps). For example, the average lasing threshold for a GaN nanowire under femtosecond excitation is ~500 nJ/cm², whereas P_{th} for a similar GaN nanowire under nanosecond excitation is ~150 μJ/cm². The higher lasing threshold with
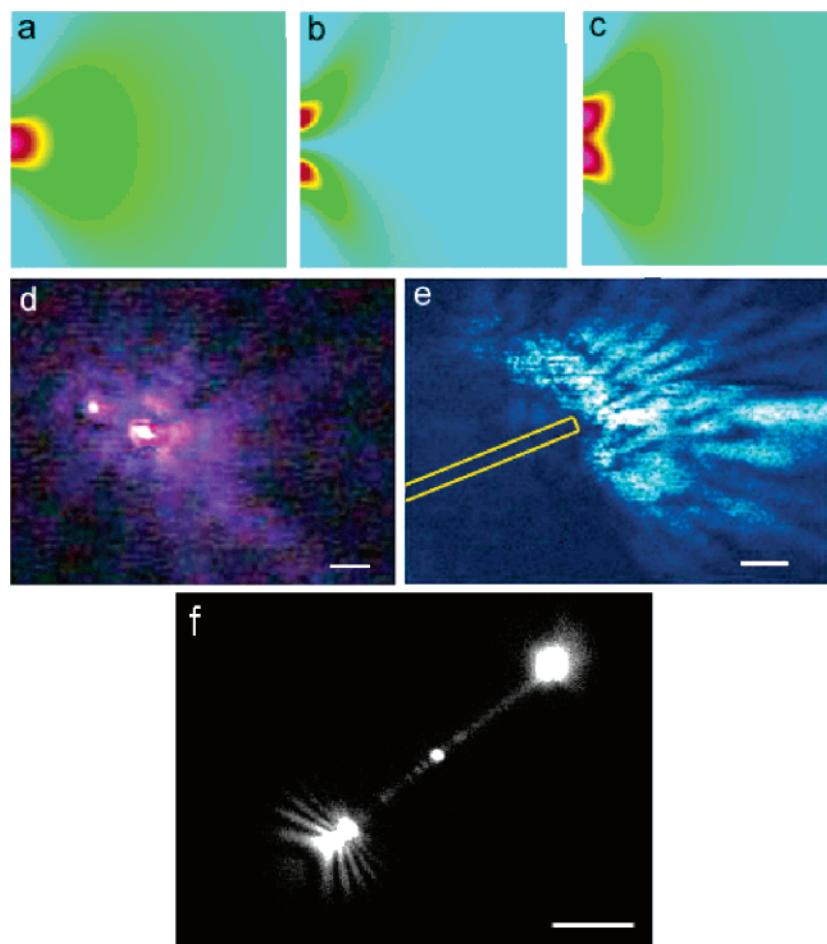
Figure 10. Far-field and near-field emission patterns from lasing ZnO and GaN nanowires. (a−c) Simulation of the Gaussian electromagnetic field emission profile from a nanowire including the (a) zeroeth order, (b) first order, and (c) summation of the two. The nanowire is horizontally oriented so that its right end facet hits the left edge of the simulation window. (d) Far-field emission pattern of a lasing ZnO nanowire. Scale bar = 3 μm. (e) Near-field optical image of a lasing ZnO nanowire showing distinct angular projection of the emitted light. The yellow outline locates the position of the nanowire (determined by NSOM, topography). Scale bar = 500 nm. (f) Far-field emission pattern of a lasing GaN nanowire showing a complex intensity distribution from one of the end facets. Scale bar = 10 μm. Reproduced with permission. Copyright 2003 American Chemical Society.

nanosecond pumping is due to the large number of decay and recombination events that occur during the duration of the pulse, therefore decreasing the degree of population inversion.

The quality-factor, or Q-factor, is a reliable means of determining the feedback in a resonant cavity. In general, the Q-factor is defined as $Q = 2\pi$(stored energy)/(energy loss), which is a measurement of the dampening of bound modes. For resonant cavities, the Q-factor can be simply expressed as $Q = \nu/\Delta\nu$, where ν is the lasing frequency and $\Delta\nu$ is the line width (fwhm) of the lasing mode. Stimulated emission line widths for ZnO nanowires typically vary between 0.25 and 1.0 nm, corresponding to Q-factors of 400−1500. Similar Q-factors are measured for the GaN nanowires. For a Fabry−Perot resonator with reflectivity of 0.19, a length of 10 μm, the line width would follow the expression

$$\Delta\nu = -c/(4\pi Ln)\ln[R^2(1 - T_i)^2] \qquad (7)$$

where T_i is the internal losses and R is the end facet reflectivity; giving a line width on the order of 1 nm. This is in good agreement with the experimental values. The larger mode width observed in some of the lasers is caused by nonzero losses (i.e., diffraction, scattering, poor end facet, etc.).

5.2. Stimulated Emission Polarization. Depending on the orientation of the optical axis of the crystal (*c*-axis in the wurtzite

crystal) with respect to the growth axis, bound cavity modes can experience differences in optical gain (transverse or longitudinal) due to various polarizations of the lasing modes. In general, the most significant modes in the nanowire cavity (radius < 100 nm) that can support lasing are the fundamental hybrid (HE$_{11}$) and transverse (TE$_{01}$ and TM$_{01}$) modes.[115] The lowest-order transverse electric and magnetic modes contain three field components and no dependence on θ (see Figure 1), whereas the hybrid mode contains all six components and has $\cos n\theta$ and $\sin n\theta$ dependence.[114]

It is arduous to eliminate all substrate effects on the polarization of lasing modes, however, the polarization can be analyzed by rotating a polarizer in the optical path, rotating the nanowire in a fixed excitation polarization, or by rotating the excitation beam.[102] Figure 9a shows a spectrum of a lasing ZnO nanowire with distinct modes that do not respond to a rotation of the collection polarization (ρ_x <0.03). These modes are likely the lower-order transverse electric (TE) and/or transverse magnetic (TM) modes. In contrast, there are modes that show a distinct polarization along the plane of the substrate with $\rho_x = 0.27$ and 0.18. These are likely the fundamental hybrid HE$_{11}$ or even the HE$_{12}$ modes.

Polarization along the *x*-axis can also be observed if the nanowire is rotated with respect to a fixed detection polarization and an unpolarized excitation. Figure 9b,c displays results
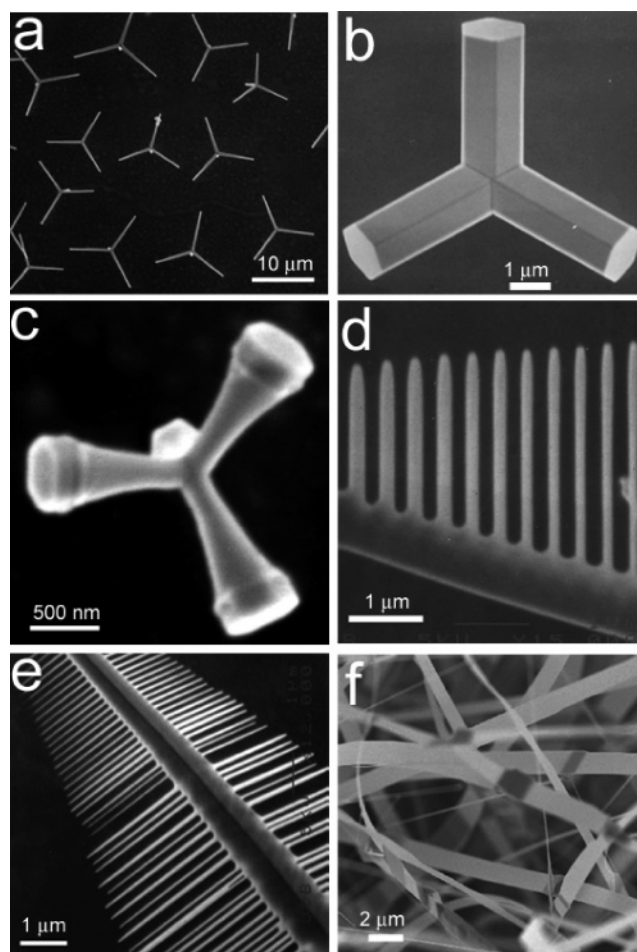
Feature Article

J. Phys. Chem. B, Vol. 109, No. 32, 2005 **15201**
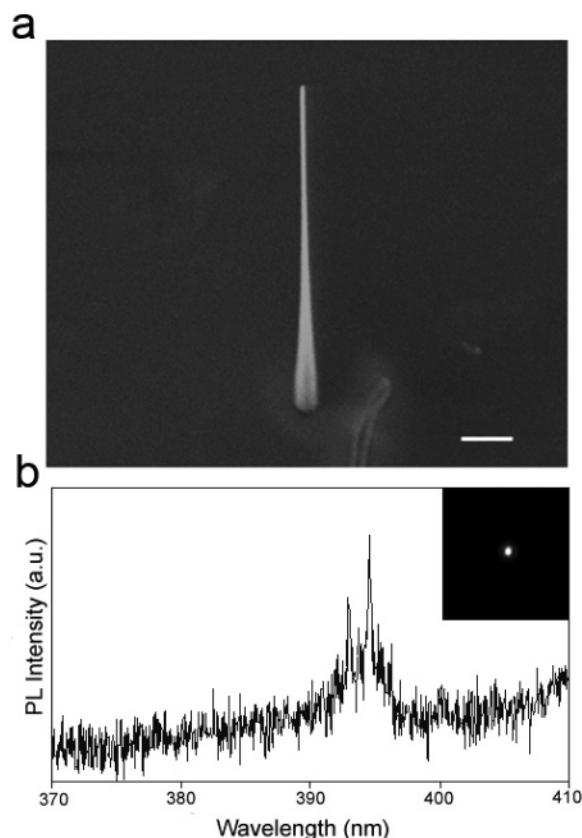
Figure 11. (a) A SEM image of a single vertical ZnO nanowire grown on sapphire. Scale bar $= 1$ μm. (b) Stimulated emission spectrum from an individual vertical nanolaser generated from a nanosecond excitation source (266 nm, 8 ns). Inset: A top-view PL image of the lasing nanowire.

Figure 12. A collage of different ZnO cavity shapes including (a) small tetrapods (arm diameter: 50−300 nm), (b) large micron sized tetrapods (arm diameter: > 500 nm), (c) trumpeted tetrapods, (d,e) dendritic and comblike structures, and (f) nanoribbons. Stimulated emission has been demonstrated in all of these cavity shapes.

obtained from the same wire after rotating the long axis by 90°. As predicted, the HE_{11} mode shows the highest polarization and experiences gain at the lowest excitation power (Figure 9b, inset). After rotating the nanowire laser 90°, additional modes emerge with similar polarization, signifying identical component modes. After rotating the nanowire, the hybrid mode still has the dominant polarization memory; however, all the lasing modes now have significant polarization dependence. In this excitation geometry (Figure 9c) it appears as though the substrate is having a greater influence on the transverse guided modes, though their polarization memories are still smaller than the hybrid components.

Alternatively, a polarized excitation can be used to preferentially excite specific bound modes. For a particular wire excited with a polarized beam oriented at $\phi = 90°$ (Figure 9d), the HE, TE, and TM modes are all excited, with the HE_{11} identified as the mode showing the largest polarization memory. By rotating the excitation polarization 90° (parallel to substrate plane), only the axial components are excited. The TE modes would theoretically be weakly excited in this configuration due to poor coupling of these modes to the axial direction (Figure 9d, inset). To re-excite the TE modes and quench the TM modes, the incident bean can remain polarized in the plane of the substrate and the axis of the nanowire need only to be oriented along the incident plane of the laser.[102]

As the guided modes in a nanowire cavity propagate along the *z*-axis, the guided wave eventually hits the end facet of the wire. At this point, a small portion of the wave is reflected back into the cavity, while the rest is radiated outward. Due to the various symmetries of the guided modes, the resulting far-field emission pattern can be extremely complex. Theoretical simula-

tions using the finite-difference time-domain (FDTD) method in cylindrical coordinates show distinct emission patterns for the lowest order HE, TE, and TM modes.[115] Although the simulations were done for a nanowire with a dielectric constant ($\epsilon = 6$) and band gap energy (3.3 eV) similar to GaN, the results are insightful for other systems, such as ZnO, because of the close match in band gap and dielectric at the lasing frequencies. In the theoretical simulations, the transverse modes were found to have zero emission at $\phi = 0$, which is directly related to the symmetry of the modes, and a maximum lying between 30° and 50°. Interestingly, the authors found little change in the angular emission of the TE_{01} mode as the radius of the nanowire was increased. For the TM_{01} mode, however, there is an appreciable increase in the backward angles ($\phi > 90°$), with a simultaneous decrease in the forward angles ($\phi < 90°$), as the radius is increased. Similarly, in the HE_{11} there is an increase in the total power emitted in the backward directions as the cross-sectional dimensions of the wire are increased. Opposite the transverse modes, however, the HE_{11} mode has its maximum emission at $\phi = 0$.

Experimentally, far-field emission patterns can be more complex due to multiple modes lasing at the same frequency, the large numbers of supported modes within the cavity, external interference effects, and substrate coupling effects. The angular emission patterns from a lasing ZnO and GaN nanowire are shown in Figure 10d−f, along with a simulation demonstrating the emission pattern from a zeroth and first-order Gaussian
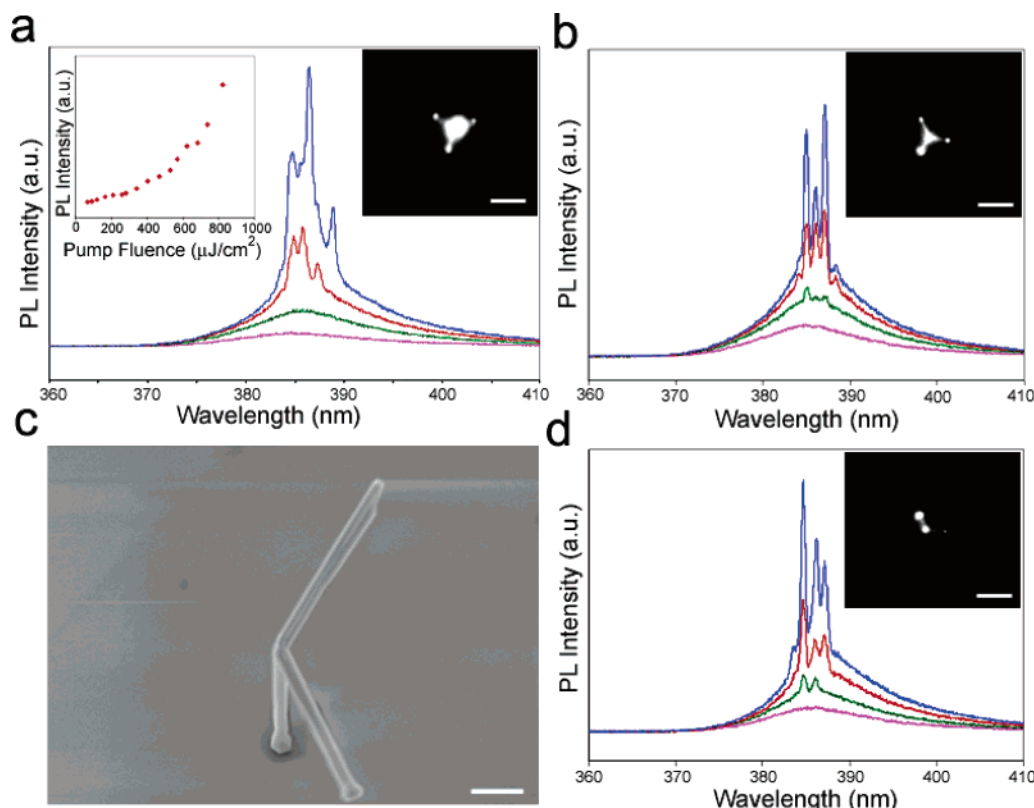
Figure 13. ZnO tetrapod manipulation and lasing in various configurations. (a) Spectra recorded at 91, 284, 468, and 738 μJ/cm^2, showing stimulated emission in the three-arms-down configuration. Inset (left): Power dependence curve showing a lasing threshold of ~430 μJ/cm^2. Inset (right): PL image of the lasing tetrapod depicting the vertical arm as a bright spot in the middle of the structure. Scale bar = 5 μm. (b) Spectra recorded at 255, 454, 596, and 766 μJ/cm^2 after flipping the tetrapod into the three-arms-up configuration. The lasing threshold for this geometry increased to ~520 μJ/cm^2 and the mode shape was drastically altered in comparison to (a). Inset: PL image of the lasing tetrapod. Scale bar = 5 μm. (c) A SEM image of the same tetrapod in (a), (b), and (d), after removing one of the arms with the micromanipulator. Scale bar = 1 μm. (d) Lasing spectra of the three-arm tetrapod shown in (c). The mode structure is similar to (b), but the lasing threshold increases further to ~584 μJ/cm^2. Inset: PL image of the lasing tripod showing larger scattering loss from the left (top arm in SEM image), damaged arm. Scale bar = 5 μm.

electromagnetic field profile (Figure 10a−c). Simple diffraction at the end facets would result in a quasi-cone of intensity spread out according to $\phi = \lambda/\pi r$. However, interference effects that occur outside of the cavity can further complicate the resulting emission pattern as seen in the near-field emission pattern of the ZnO nanowire laser and the far-field emission pattern of the GaN nanowire laser.

5.3. Cavity Shapes. All of the optical experiments described in the previous section were performed on nanowires that were physically cleaved (via sonication or dry transfer) and laid horizontally on a support substrate. During the transfer process, it is possible to damage the cavity. In subsequent experiments, the damaged cavities typically show high lasing thresholds or only spontaneous emission. In addition, the wire/substrate interface increases propagation losses by directing some of the propagating field intensity into the substrate. This leads to a lower Q-factor and may perturb mode polarization, reflectivity, and/or gain.

One solution to this problem is to grow dilute nanowire arrays and probe the optical properties of individual wires standing on their growth substrates. This approach avoids potential intercavity coupling and enhances the gain properties of the resonator through a minimal interaction with the substrate. This vertical configuration also correlates well with the geometry used in most theoretical models.[114−116,129] Dilute arrays (wire spacing > 20 μm) of ZnO nanowires were synthesized on sapphire substrates decorated with a low density of gold colloids that were applied by spin-coating. The SEM image in Figure 11a displays an isolated ZnO nanowire in the dilute array. The

micrograph provides evidence that the tapered cavity is not an ideal FP resonator, but nevertheless the tapered base provides enough optical feedback to promote stimulated emission (Figure 11b). Gaining position control of the free-standing cavities and optimizing their surface morphologies and dimensions could open up novel applications for these materials in studying quantum optics as well as other quantum electrodynamic phenomena.

Part of the synthetic toolbox for growing nanomaterials is the ability to control size and shape of the nanocrystal,[12,130] which can often lead to novel structures with various optical and electronic properties. Figure 12 provides an overview of some of the ZnO structures produced by a simple evaporation and condensation synthesis using different Zn sources and oxygen partial pressures.[131] All of these structures, including the tetrapods, nanoribbons,[132] and dendritic structures[45] can produce stimulated emission and act as lasers. For example, the nanoribbons and dendritic comb structures show lasing thresholds (under fs pulses) of ~3 mJ/cm^2 and ~700 nJ/cm^2, respectively. Compared to the nanowire cavities, the nanoribbon and dendritic structures have much higher lasing thresholds. This is attributed to the higher roughness factors of the resonating cavities (lower Q). Further optical characterization of these two structures will not be discussed here. Additional information can be found in the cited references.

One cavity shape that has not been studied optically, only structurally, is the tetrapod.[131] The tetrapods are fully tetrahedral structures with the symmetry of the methane molecule. The smallest tetrapods have arm lengths of 3−5 μm and average

Feature Article

J. Phys. Chem. B, Vol. 109, No. 32, 2005 **15203**

arm diameters of ~150 nm (Figure 12a). At low pump fluences (femtosecond: <1 μJ/cm^2; nanosecond: <200 μJ/cm^2) the spontaneous emission dominates, showing a broad featureless line shape (Figure 13a). Typical lasing thresholds range from 1 to 5 μJ/cm^2 and 200−500 μJ/cm^2 under femtosecond and nanosecond excitation, respectively. Photoluminescence images show that the arm cavities strongly waveguide the band edge emission with little detected emission from the side surfaces or core (Figure 13a,b inset). Since the tetrapod structure is a complete 3D cavity, it provides a model system to begin studying cavity effects caused by the substrate and mode coupling between adjacent arms.

The tetrapods tend to rest on a surface either on three arms or on one arm, with about equal frequency. In this way they are unlike children's toy jacks, which always fall on three arms. We can use a commercial micromanipulator to flip individual tetrapods from one configuration to the other and thereby study the lasing behavior. Figure 13 shows data from a tetrapod with arms 3.8 μm long and 280 nm in diameter. The optical images in the insets were captured after pumping the tetrapod above its lasing threshold. The images show the expected emission intensity pattern for the two resting configurations. When the tetrapod rests on three arms, all four arms are visible. The arm that is directed toward the objective (center of tetrapod) appears brightest because its emission is collected most efficiently by the microscope. When three arms are pointing up, the fourth arm cannot be seen since it is obstructed from view by the convergence of the other three arms. There is a slight increase in emission intensity at the center of the tetrapod (visible to the camera when three arms are up) as a result of scattering from where the four arms connect. Previous transmission and scanning electron microscopy experiments show that there are distinct grain boundaries around the tetrapod core that can cause the observed scattering.[131]

The lasing threshold for the three-arms-down configuration was determined from the power curve to be ~430 μJ/cm^2. This is slightly lower than the threshold for the three-arms-up (~520 μJ/cm^2), which is likely caused by a decrease in collection efficiency and/or larger losses at the substrate/ZnO interface formed by the arm pointing down. The mode structure is also dramatically different between the two resting geometries. The modes appear distinctly separated and stable in the three-arms-up configuration, but become more washed out in the three-arms-down configuration. Since the spectra in this experiment are being captured over multiple pulses (~100 pulses), any mode fluctuations will cause a flattening in the resulting line shape. Further experiments are needed to better understand the nature of the mode fluctuations, but certainly substrate coupling, inter-cavity coupling and collection geometries could all be contributing to the complex mode variations.

Since the tetrapods are 3D cavities, it will be interesting to study the coupling effect between adjacent arms. The arms either form a single cavity mode or resonate as independent cavities. One promising approach to disrupt the cavity is to use a micromanipulator to remove individual arms. The SEM image in Figure 13c captures the resulting shape after one of the arms from the tetrapod in Figure 13a,b is detached. It is apparent that one of the cavities was damaged during the manipulation step, which partly explains the stimulated emission image in the inset of Figure 13d. Even with the one arm removed, and a third arm damaged, the lasing threshold increases only slightly to ~580 μJ/cm^2. In addition, the mode structure does not change considerably from the undamaged tetrapod in Figure 13b. These
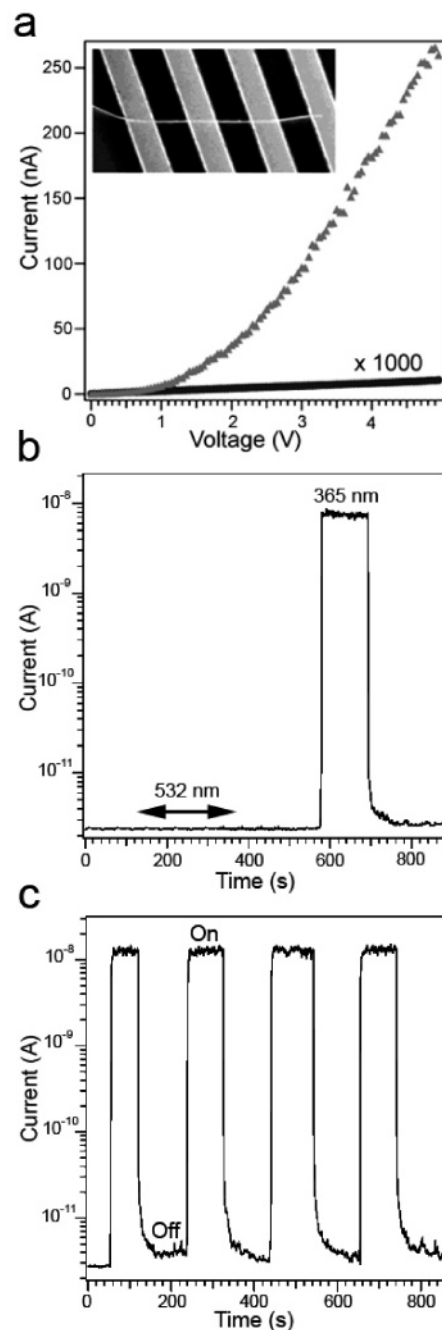
Figure 14. Current−voltage characteristics and optical switching of a single ZnO photodetector. (a) I−V plot recorded in the dark (black circles) and under 0.3 mW/cm^2 (365 nm) of illumination (gray triangles). Inset: A SEM image of the device showing a 60 nm diameter nanowire across four Au electrodes. (b) Photocurrent time course of a ZnO nanowire photodetector showing the wavelength selectivity between sub-band gap 532 nm light and above-band gap 365 nm illumination. (c) Photocurrent time course illustrating the reversible switching between "on" and "off" states. The "on" state was generating by illuminating the nanowire with above-band gap light (365 nm, hand-held UV lamp). The voltage potential was held constant at 1 V in both (b) and (c). Reproduced with permission. Copyright 2002 Wiley-VCH Verlag GmbH.

results suggest that the arms of the tetrapod might behave as independent cavities, although some degree of intercavity coupling likely plays a role on the bound modes. Additional decoupling experiments on the tetrapods, as well as manipulating free-standing nanowire cavities into model coupling geometries, should provide more insight into how adjacent cavities affect mode structure.
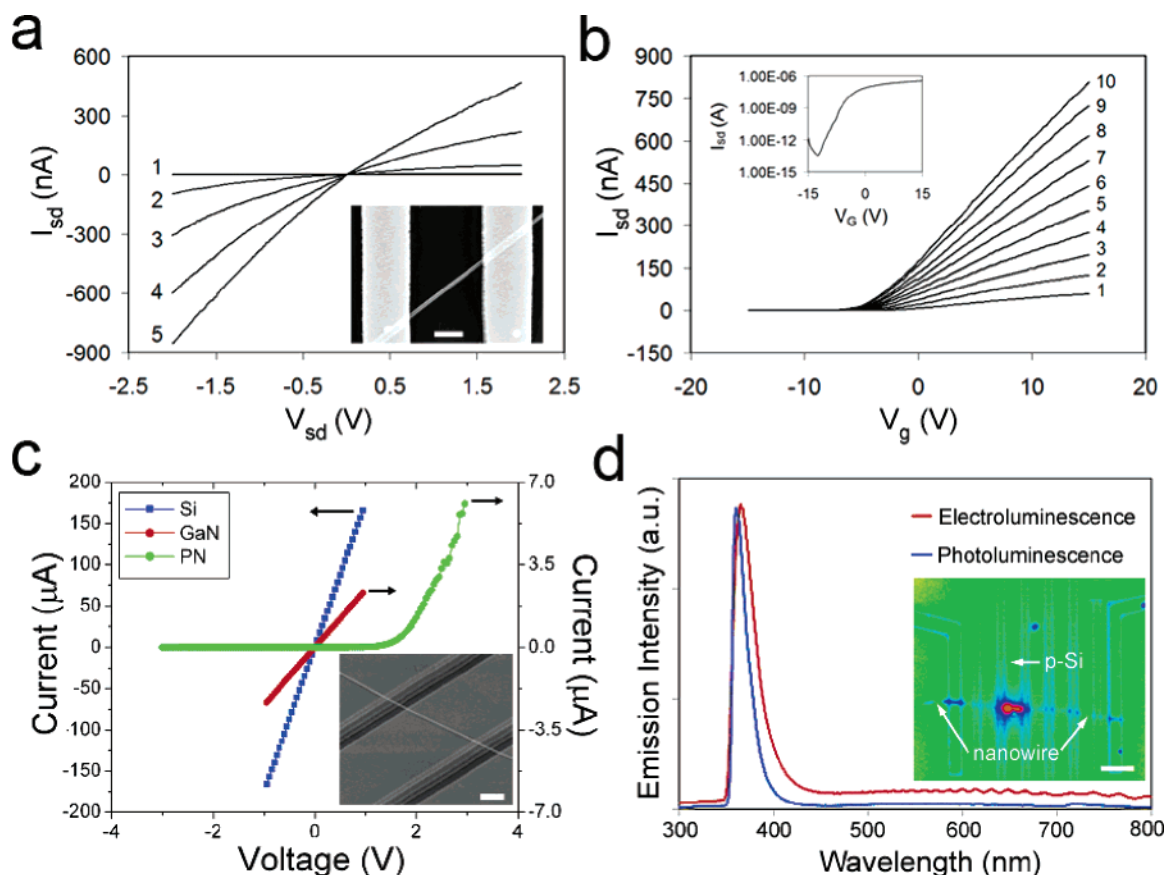
Figure 15. Electronic and optical properties of a nanowire FET and p−n diode. (a) Current−voltage properties of a 101 nm ZnO nanowire FET. Traces 1−5 correspond to gate voltages of −10, −5, 0, 5, and 10 V, respectively. Inset: SEM image of the device. Scale bar = 1 μm. (b) Transconductance properties of the same device plotting the source−drain current as a function of gate voltage. Traces 1−10 correspond to source−drain biases of 0.1, 0.2, 0.3, 0.4, 0.5, 0.6, 0.7, 0.8, 0.9, and 1.0 V, respectively. Inset: Logarithmic plot of the source−drain current vs gate voltage showing a threshold voltage of ~12 V. The V_{sd} was held constant at 0.5 V. (c) Current−voltage plot of a GaN nanowire LED (Si-line: blue; GaN wire: red; p−n diode: green) recorded at 5 K. Inset: SEM image of the GaN across multiple p-Si lines. Scale bar = 2 μm. (d) Electroluminescence and photoluminescence spectra of the same GaN nanowire LED. Spectra were recorded at 5 K with a V_{sd} of 10 V. Inset: Pseudo-color darkfield/PL image showing the strong UV emission (bias = 10 V) at the p−n junction created by crossing a GaN nanowire (horizontal) and p-Si line (vertical). Only one p-Si line is turned on (arrow). Scale bar = 10 μm.

Beyond the homogeneous compound nanowire lasers, there exist core−sheath nanowire heterostructures that provide a unique geometry for applications requiring miniaturized light emitters. We recently demonstrated UV lasing from optically pumped GaN/Al$_x$Ga$_{1−x}$N core−sheath quantum wires.[133] Phase separation during the VLS process leads to cylindrical GaN cores with diameters as small as 5 nm surrounded by a 50−100 nm-thick cladding composed of Al$_{0.75}$Ga$_{0.25}$N. Normally, GaN nanowires with diameters less than ~100 nm are too leaky to sustain laser cavity modes. However, surrounding slender GaN wires with a material of larger band gap and smaller refractive index creates a structure with simultaneous exciton and photon confinement. The result is a GaN core size that is comparable to the Bohr radius of the exciton for GaN (11 nm) and a core band gap (GaN, 3.42 eV) smaller than that of the sheath (Al$_{0.75}$Ga$_{0.25}$N, 5.25 eV). Both factors in this unique core−sheath nanostructure lead to the effective carrier/exciton confinement. When optically pumped, the core provides a gain medium while the sheath acts as a Fabry−Perot optical cavity. Soon, robust assembly methods appropriate for a larger variety of materials will enable the use of injection nanolasers in sensing, optical communications and probe microscopy.

6. Nanowire Photodetectors, FETs, and LEDs

Equally important to light generation in nanoscale structures is efficiently detecting optical inputs and processing them as electrical outputs. Creating electrical switches on the nanometer scale has been successfully demonstrated using a global back gate geometry similar to that used in nanotube transistors.[134−136] Using this design, a host of nanowire electronic devices have been made which now include field effect transistors (FETs), p−n junctions, bipolar junction transistors, complimentary inverters, and resonant tunneling diodes.[31,33,39,40,137−139] For nanowire photodetection, a nanowire is configured to monitor the photocurrent as a function of excitation. In this scheme, a constant bias across the nanowire is applied, and instead of using a gate to induce current fluctuations, an optical flux forces the wire from an insulating to a conducting state. This type of layout can be termed a linear nanowire photodetector since the photocurrent is proportional to the number of carriers produced within the semiconductor by an optical absorption process.

Nanowires are fabricated into a horizontal FET configuration either by dispersing them on pre-patterned metal electrodes (wire-on-electrode; Figure 14a, inset) or by using electron beam lithography to define electrodes on dispersed wires (electrode-on-wire; see Figure 15a, inset). Some early work in our group showed that ZnO nanowires configured as a FET act as excellent photodetectors to wavelengths shorter than the band gap of ZnO.[35] The nanowires were insulating (>3.5 MΩ·cm) in the dark state and became conductive under UV exposure, with up to a million times lower resistivity under illumination. Figure 14a shows the current−voltage (I−V) characteristics of a ZnO

Feature Article

J. Phys. Chem. B, Vol. 109, No. 32, 2005 **15205**

nanowire (diameter ~60 nm) dispersed on four terminals in the dark and under illumination from a hand-held UV lamp (0.3 mW/cm^2 at 365 nm). Measurements were carried out using a Keithley source-measure unit at room temperature. The large increase in current is observed only when resonant excitation wavelengths shorter than the band gap (~370 nm) illuminate the wire, making the ZnO detector an excellent optical switch (Figure 14b,c).

Previous experiments with ZnO crystals and thin films have shown that the chemisorption of oxygen-containing molecules can play a large role in making a nanowire conductive or insulating.[140-142] A similar mechanism has been proposed to occur in the ZnO nanowires. In the dark (and in air), the oxide wire surface contains adsorbed oxygen (O_2), or other oxygen-containing molecules, that uptake free electrons from the n-type ZnO [$O_2(g) + e^- \rightarrow O_2^-(ad)$] and form a negatively charged surface passivation layer. Once electron–hole pairs are generated by the absorption of a photon, the holes migrate toward the passivation layer and recombine at the surface to discharge gaseous oxygen [$h^+ + O_2^-(ad) \rightarrow O_2(g)$]. The remaining electrons increase the total number of free carries and lower the resistance across the wire. Using this type of surface-mediated conductivity, the sensitivity of the photodector should be enhanced by increasing the surface-to-volume ratio. It will be important for future optoelectronic devices to continue developing linear nanowire photodetectors based on chemical gating as well as other detector systems (i.e., nonlinear) such as avalanche detectors.

Driving current across a nanowire FET, instead of detecting current fluctuation, forms the basis of electrical computation and light emission using nanowire assemblies. The $I-V$ properties of a single n-type nanowire FET are shown in Figure 15a,b.[143] The source–drain current (I_{sd}) vs voltage (V_{sd}) plots are generally linear up to 2 V, suggesting good electrical contact between the wire and metal electrodes (contact resistances are $2.1 \times 10^{-3} - 1.6 \times 10^{-2}$ Ω·cm). As expected for an n-type semiconductor, the conductance increases with increasing gate voltage (Figure 15b). By crossing a p- and an n-type material, and forming an effective depletion layer, the FET layout can be configured as a light emitting diode (LED). In general the geometry consists of an n-type nanowire crossing p-type nanowire or support substrate, or by creating a radial core–sheath nanowire.[33,37-40] The $I-V$ properties of a GaN nanowire p–n junction are shown in Figure 15c. Here an n-type GaN nanowire lays across multiple p-Si lines to form an array of p–n diodes. The turn-on voltage for the p–n diode is ~1.5 V and shows strong UV electroluminescence when driven above the threshold voltage. With our current manipulation capabilities it should be possible to form more complex diode assemblies that couple LED emission into passive optical elements (see below) to perform all-on-a-chip optical spectroscopy and high-throughput screening of chemical or biological species.

7. Passive Optical Elements

Central to the development of nanoscale optoelectronic devices is the manipulation of photons in structures smaller than the wavelength of light. Subwavelength waveguides provide the key to performing tasks such as computing, communication, and sensing at or below the diffraction limit. In the previous sections (section 5 and 6), active optical elements (lasers, LEDs, and photodetectors) were discussed as promising components in future integrated nanophotonic circuits. To perform logic operations in future photonic devices, however, photons generated by nanowire sources (lasers or LEDs) must be efficiently
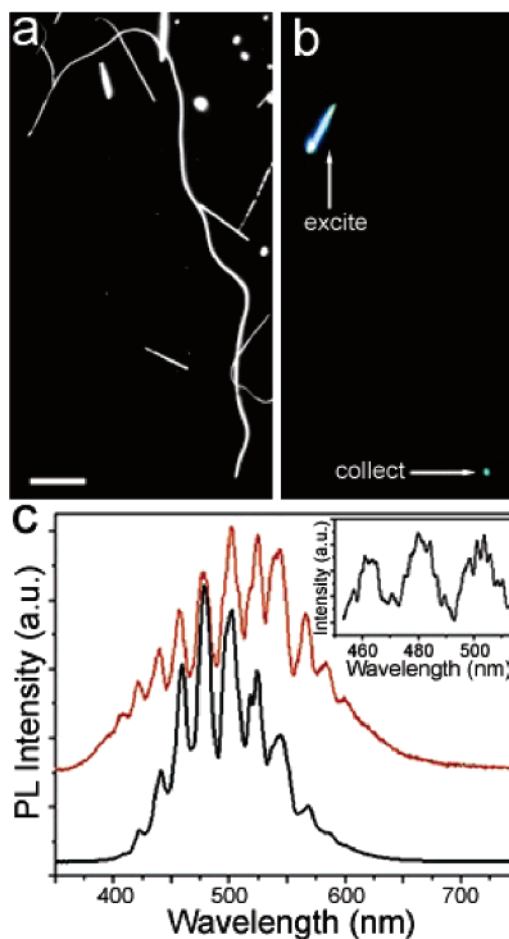
Figure 16. Waveguiding in a 715 μm long SnO$_2$ nanoribbon (cross-section: 350 nm × 245 nm). (a) Dark-field image of the ribbon after dry transfer to a silica surface. Scale bar = 50 μm. (b) True color PL image of the ribbon after exciting one end with the 325 nm laser. The defect PL is efficiently guided to the opposite end terminal. (c) Far-field spectra (red: 300 K; black: 5 K) of the waveguided emission after it makes its transit through the SnO$_2$ cavity showing complex modal structure arising from the cavity shape and geometry. There is minimal dependence of the mode structures on temperature (i.e., changes in refractive index). Spectra are offset for clarity. Inset: High-resolution spectrum of the three central peaks (at 5 K) showing additional fine structure. Reproduced with permission. Copyright 2004 American Association for the Advancement of Science.

captured and precisely delivered to the various components of an optical chip, including detectors, filters, and switches. Routing of the optical signal can be achieved by coupling passive subwavelength waveguides directly to the active elements. In contrast to lithographically defined waveguides,[8,144] chemically synthesized nanowires can be prepared as free-standing entities from a variety of materials. However, assembling them as specific functioning components in a photonic device remains a challenge. The following section provides an overview of recent efforts of our group to build nanowire photonic architectures and find novel applications for these materials in microfluidics and biology.

7.1. Subwavelength Oxide Waveguides. Nanoribbons of binary oxides exhibit a variety of interesting properties including extreme mechanical flexibility, surface-mediated electrical conductivity,[36] and stimulated emission.[132] Tin dioxide (SnO_2) nanoribbons have recently been shown to act as excellent subwavelength waveguides of UV and visible light.[145] SnO_2 is a wide band gap semiconductor (3.6 eV, direct but dipole forbidden) that finds application in gas sensing and as transpar-
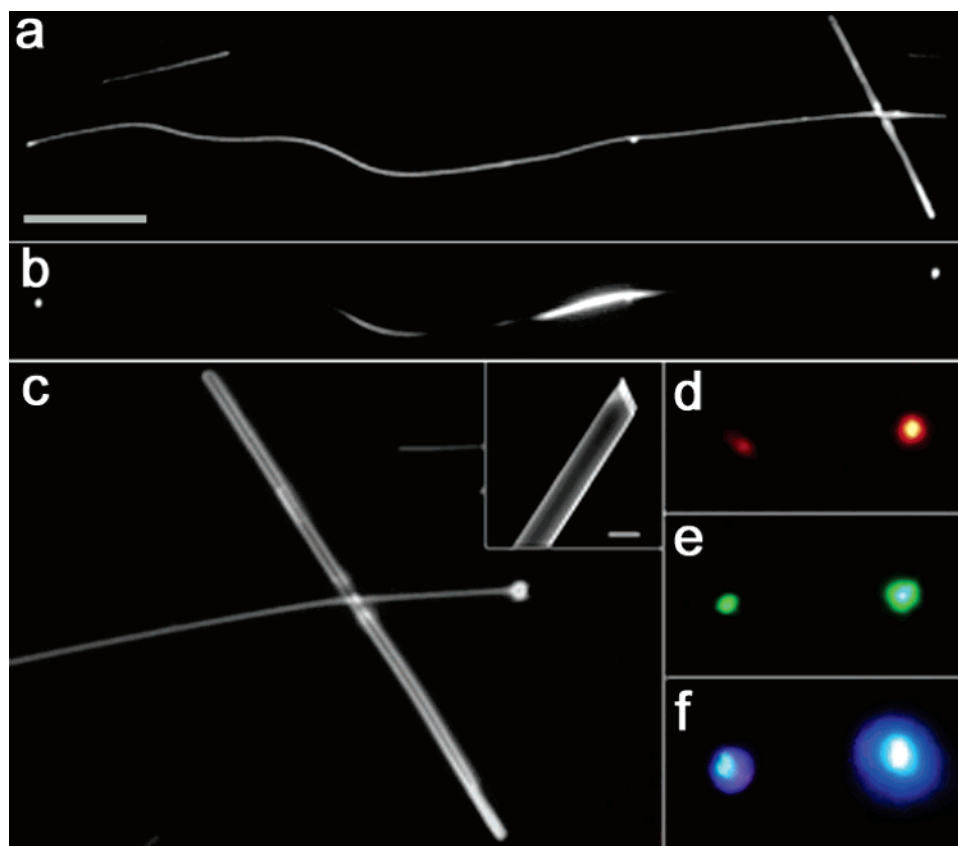
Figure 17. Panchromatic waveguiding in a SnO$_2$ nanoribbon (425 μm × 520 nm × 275 nm). (a) Dark-field image of the ribbon supported by a silica substrate. Scale bar = 50 μm. (b) PL image with the 325 nm excitation focused near the middle of the ribbon showing strong waveguiding to both ends. (c) Zoom in dark-field/PL image of the right end terminus while the UV laser is focused on the opposite end. A wide (∼1 mm) ribbon lies across the primary ribbon waveguide. Inset: An angled SEM image capturing the rectangular cross-section of one of the ends of the nanoribbon. Scale bar = 500 nm. (d−f) True color images (taken at the right terminus) of monochromatic 652, 532, and 442 nm light waveguiding through the ribbon. The dimmer emission spot is caused by the overlap with the thick ribbon. The nonresonant excitation was generated from diode lasers that were focused on the leftmost terminus. Reproduced with permission. Copyright 2004 American Association for the Advancement of Science.

ent electrodes. The ribbons possess fairly uniform (± 10%) rectangular cross sections (see Figure 17c, inset) with side dimensions as large as 2 μm by 1 μm and as small as 15 nm by 5 nm. However, most of ribbons (> 80%) have dimensions between 100 and 400 nm, an optimal size range to efficiently guide visible and UV wavelengths in a subwavelength cavity ($n \sim 2.1$ for these wavelengths). The ribbons can be synthesized in milligram quantities and can have lengths greater than 3 mm. SnO$_2$ luminesces as two broad defect bands centered in the green (2.5 eV) and orange (2.1 eV), such that its emission spans most of the visible spectrum.

Once individual ribbons are transferred to a silica surface (n = 1.45), a HeCd laser (3.8 eV) can be focused on one of the ends to generate PL that is strongly guided to the opposite end (Figure 23). The waveguiding essentially mimics a conventional fiber optic. The ribbon in Figure 16a is 715 μm long, 350 nm wide, and 245 nm thick. Interestingly, the far-field spectrum collected at the far end of a ribbon shows a distinct quasi-periodic modulation resulting from wave interference within the cavity. The mode structure is not longitudinal (eq 3) in nature, as in shorter nanowires (section 5), but is likely caused by transverse modes that are highly dependent on cavity shape, cross-sectional dimensions, substrate coupling, and variations in refractive index.

Nonresonant waveguiding (i.e., sub-band gap light) in these structures can be achieved by focusing laser diodes on one end of the nanoribbon. Figure 17 displays a 425 μm long ribbon (520 nm × 275 nm) with a wide (∼1 mm) ribbon across one of the ends. Monochromatic red, green, and blue light is injected into one end of the long ribbon (at the left) and exits at its distant end (on the right) (Figure 17d,f). One would expect the shortest wavelengths to be confined better than longer wavelengths for a given cavity size, shape and geometry (eq 5).[99] If the ribbons are treated as cylindrical waveguides surrounded by air, calculated cutoff diameters for higher order optical modes are approximately 270, 220, and 180 nm for 652, 532, and 442 nm light. These approximations are in reasonable agreement with the sizes (determined by SEM) of the nanoribbons used here, even though they assume a simplified geometry and ignore substrate-induced losses and other effects.

The color of the waveguided light can be used to predict the size of the nanoribbon when white light (SnO$_2$ PL) is launched down the cavity. For example, larger ribbons emanate white, whereas the small nanoribbons appear blue due to the higher losses at the longer wavelengths. As a result, the ribbon waveguides act as excellent short pass filters. Wavelength cutoffs spanning from 450 to 600 nm have been identified (Figure 18a) by determining the 50% transmission point of the ribbon. Wavelengths longer than the cutoff are virtually eliminated (zero transmission) from the cavity.

To quantify the propagation losses, a near-field setup can be employed to locally collect the waveguided light as a function of pump/probe distance (see section 2). Loss measurements were performed on ribbons of various sizes supported on a silica surface. Losses were ∼10 db/cm for wavelengths between 400 and 550 nm with the smallest waveguides showing losses up to 80 db/cm at wavelengths of 475 nm. Even with these reported

Feature Article

J. Phys. Chem. B, Vol. 109, No. 32, 2005 **15207**
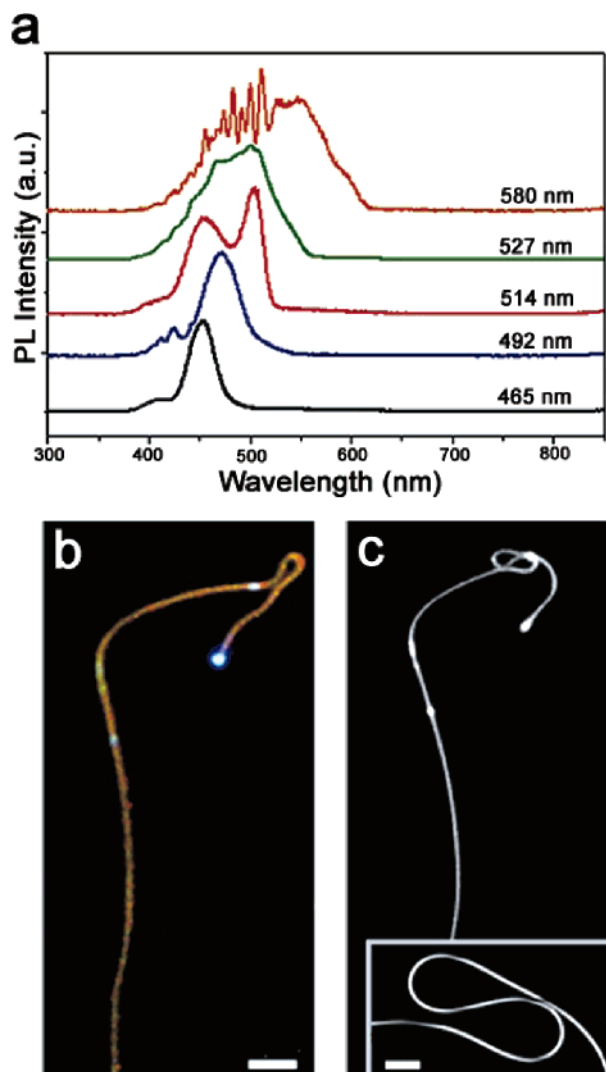
Figure 18. (a) Short pass filtering properties of different sized SnO$_2$ nanoribbons showing distinct empirical frequency cutoffs. The 50% cutoff wavelengths of 465, 492, 514, 527, and 580 nm represent cavity dimensions of 310 nm by 100 nm (0.031 μm^2), 280 nm by 120 nm (0.034 μm^2), 350 nm by 115 nm (0.04 μm^2), 250 nm by 225 nm (0.056 μm^2), and 375 nm by 140 nm (0.052 μm^2), respectively. Spectra are normalized and offset for visual clarity. (d) True color dark-field/PL image of a ∼5200 aspect ratio ribbon showing minimal effect on waveguiding after impinging a sharp curvature of radius (∼1 μm) on the structure. Scale bar = 5 μm. (c) Dark-field/PL image after fashioning two tight loops (curvature of radius for both is ∼1 μm). Blue light is effectively guided around both bends. The scattering center in the loop is caused by a small step edge rather than physical contact. Inset: A SEM image resolving the S-turn. Scale bar = 1 μm. Reproduced with permission. Copyright 2004 American Association for the Advancement of Science.

losses, however, the ribbon waveguides are able to guide light over hundreds of microns, which is adequate for most applications.

The SnO$_2$ nanoribbons are of sufficient length and strength to be manipulated on surfaces to form various shapes and multiwire assemblies. On all experimental substrates used (silicon, silica, sapphire, copper, and mica), the ribbons can be fashioned into virtually any 2D shape. This is due in part to the electrostatic forces between the substrate and ribbon that prevent elastic recoil of the structure. For example, the high-aspect-ratio ribbon in Figure 18b (dimensions: 275 nm by 150 nm by 785 μm) was shaped into a tight S turn with a radius of curvature ∼1 μm to illustrate the robust nature of the optical steering in
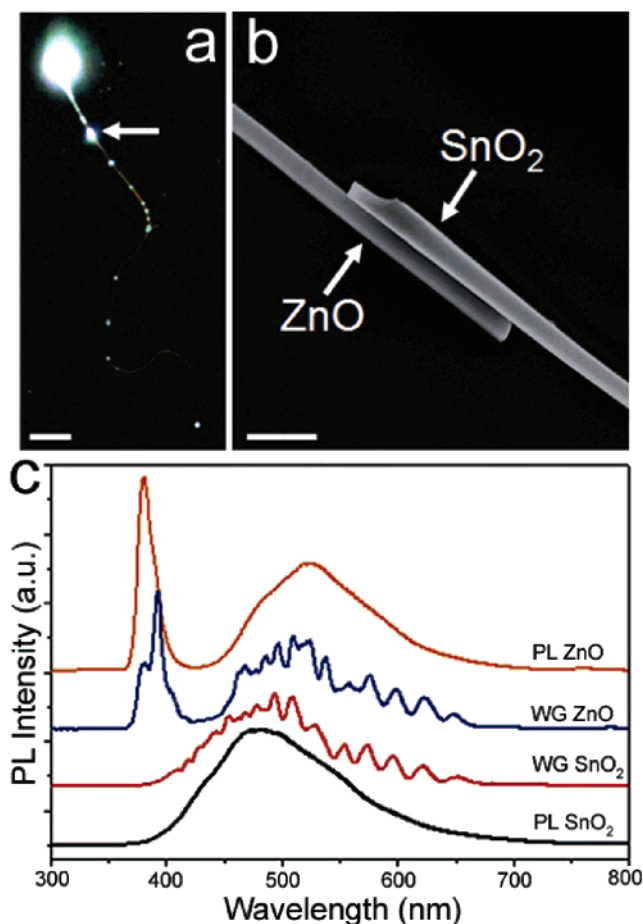
Figure 19. Creating optical junctions with nanoribbons and nanowires. (a) Dark-field/true color PL image of a heterojunction (arrow denotes junction) created between a ZnO nanowire (diameter: 300 nm; length: 56 μm) and a SnO$_2$ nanoribbon (265 μm × 700 nm × 270 nm). ZnO PL is generated with 325 nm excitation that is then launched down the SnO$_2$ cavity. Scale bar = 25 μm. (b) SEM image resolving the junction between the wire and ribbon. Scale bar = 1 μm. (c) Spectra recorded at various collection and excitation locations. Direct PL from the ribbon (black) and wire (orange) were excited and collected from the same region. The waveguided PL from the wire (blue) and ribbon (red) was collected at the bottom terminus of the ribbon after exciting each structure, respectively. Both the band edge and defect PL from the ZnO are modulated by the transit through the SnO$_2$ cavity. Reproduced with permission. Copyright 2004 American Association for the Advancement of Science.

these structures. The sharp bend induced minimal losses and no measurable decrease in the output of the waveguide was observed. In general, twists and bends with radii of 1 μm do not disrupt the optical confinement and the ability of these structures to route light across hundreds of micrometers (Figure 18c).
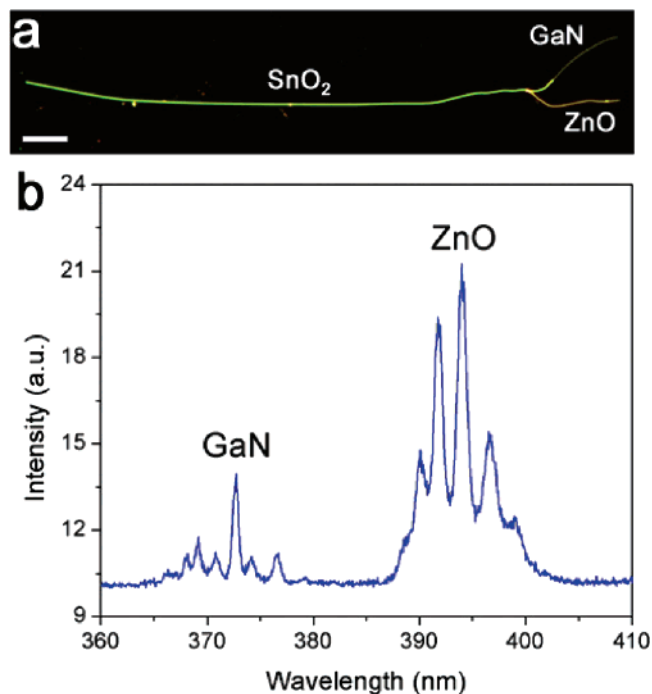
7.2. Creating Optical Networks and Assemblies. Optical linkages between active and passive components can be constructed by linking nanowires using evanescent coupling. Because light diffracts with a large cone angle at the end facets of these subwavelength cavities, it is crucial for efficient coupling to bring them into close proximity, preferably in direct contact. It was found that a staggered side-by-side configuration, in which the structures interact over a few microns, outperforms bridged or direct end-to-end coupling. Weaker coupling is achieved by staggering structures with a thin air gap (several hundred nanometers) between them, allowing communication via tunneling of evanescent waves.[146] Staggered junctions between multiple SnO$_2$ nanoribbons and nanowires (ZnO and
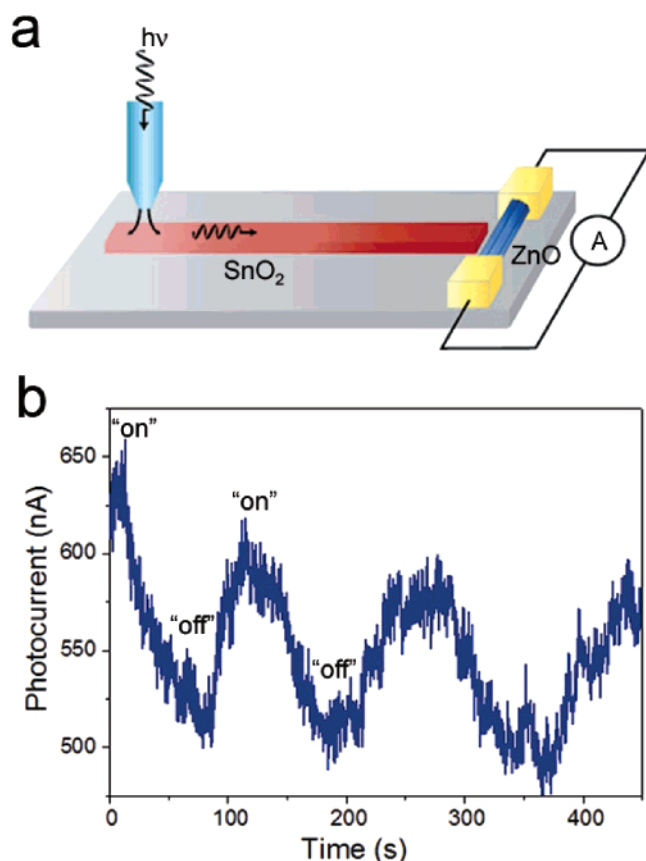
Figure 20. (a) Schematic showing the integration of light detection at a nanoribbon/nanowire interface. UV Light is launched via a NSOM probe to generate white light in the SnO$_2$ nanoribbon that is guided down the cavity to the detector. (b) Photocurrent response of the ZnO nanowire photodetector as the NSOM probe is scanned "on" and "off" of the nanoribbon cavity. Reproduced with permission. Copyright 2004 American Association for the Advancement of Science.

Figure 21. (a) Dark-field image illustrating the coupling geometry of two nanowire lasers (GaN and ZnO) to a single SnO$_2$ nanoribbon. Scale bar = 25 μm. (b) Spectra recorded at the left terminus of the SnO$_2$ nanoribbon after simultaneous nanowire laser injection at the right terminus. Both laser pulses are guided through the SnO$_2$ cavity and emerge as two resolvable packets (dictated by their band gaps) of modes. Reproduced with permission. Copyright 2005 National Academy of Sciences, U.S.A.

GaN) have been created to demonstrate the feasibility of making efficient optical linkages. In general, power transfer efficiencies exceeding 50% can be attained between cavities of equal refractive index. Model multiribbon structures have also been created, including a three-ribbon directional coupler, a four-ribbon grid, and a four-ribbon color filter (see below). With further integration, it should be possible to create more functional geometries such as branched optical hubs and Mach−Zender interferometers (optical modulators) that use the electrooptic effect for phase shifting.[1]

One such optical linkage between a ZnO nanowire (56 μm long, ~300 nm diameter) and SnO$_2$ nanoribbon (265 μm long × 700 nm wide × 270 nm thick) is depicted in Figure 19. By pumping the ZnO nanowire with 325 nm light, both band edge and green defect emission are launched into the SnO$_2$ waveguide. The ribbon imprints its mode structure on both the UV and visible light (Figure 19c). This is a demonstration that broadband, quasi-Gaussian inputs can be captured and guided through subwavelength cavities. To detect the waveguided light, a ZnO nanowire photodetector can be built near the output end of a nanoribbon to electrically detect pulses of light guided through the SnO$_2$ cavity. Figure 20 provides a schematic setup and conductance data of a nanoribbon coupled to a ZnO photodetector. In this configuration, a NSOM tip is used to locally excite the intrinsic PL of the ribbon at one end to produce an increase in the ZnO nanowire photocurrent. The photoresponse of the nanowire detector is actually caused by the small amount

of near-UV created in the ribbon, which overlaps to some degree with the band tail of ZnO (~380 nm). It should be noted that the response time for this particular photodetector is on the order of seconds. Of course high performance nanophotonic architectures will demand more efficient photodetectors and electrically driven light sources. However, these results demonstrate the feasibility of integrating passive optical structures with photodetectors and hence the use of these nanoribbons in future photonic platforms.[147]

In addition to CW inputs, laser pulses from the active cavities (ZnO and GaN) can also be routed through SnO$_2$ waveguides.[148] Figure 21 illustrates the linkage of a GaN and a ZnO nanowire laser to the same ribbon waveguide. This establishes the possibility of performing all-nanowire nonlinear wave mixing within single subwavelength cavities. The integration of high frequency electrically driven lasers with passive nanoribbon waveguides is the next step toward effectively transducing and routing packets of optical information within an optical computer or communication device.

Since the SnO$_2$ nanoribbons also act as excellent short-pass filters, they can be used in to remove longer wavelengths to produce an optical router based on input color. This has been achieved by coupling nanoribbons with various cross-sectional dimensions, each with a different cutoff frequency ranging from the blue to red, to a common multimode core waveguide. White light can be launched down the core waveguide by optically pumping with UV (325 nm) light. The shorter wavelengths then flow through the smaller ribbons with varying propagation losses, producing multicolor outputs. The routing of different color inputs is exemplified by injecting monochromatic light to activate different channels. For example, injecting red light turns on only the core waveguide, whereas blue/near-UV light turns on all channels. Assemblies such as multi-branched hubs

Feature Article

J. Phys. Chem. B, Vol. 109, No. 32, 2005 **15209**
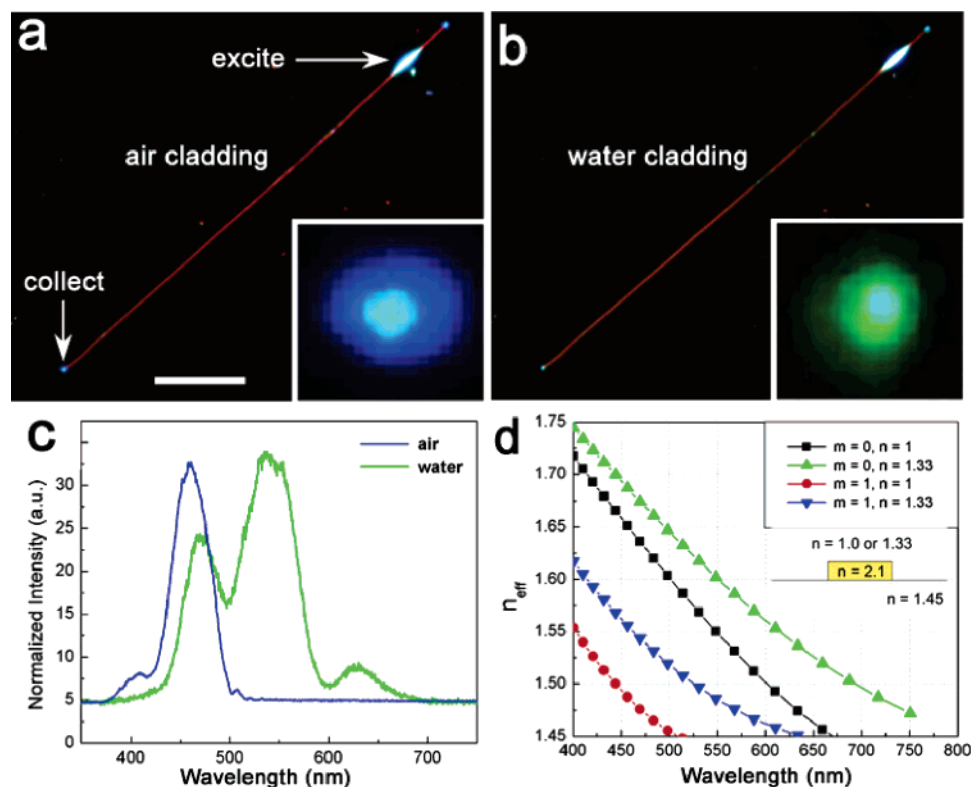
Figure 22. Waveguiding in water. (a) Dark-field/PL image of a thin nanoribbon (265 μm $\times$ 365 nm $\times$ 105 nm) waveguiding on a silica support ($n = 1.45$) with an air cover ($n = 1$). Scale bar = 50 μm. Inset: Magnified view of the end terminus showing the blue cutoff wavelength. (b) Waveguiding in the same ribbon as (a) with a water cover ($n = 1.33$). Inset: Magnified view of the end terminus showing a red shift in the cutoff wavelength. (c) Far-field spectra recorded for the air (blue) and water cover (green) showing the sharp red shift in the empirical cutoff wavelength ($\sim$480 to 570 nm) and a broadening of the line shape. The shift is caused by the decrease in refractive index between the support ($n = 1.45$) and the cover ($n = 1.33$ vs $n = 1$). (d) Dispersion curve plotting the effective refractive index, $n_{eff} = k_z c/\omega$, where k_z is the propagation wavenumber, ω is the frequency, and c is the speed of light, as a function of wavelength, for the lowest two guided modes ($m = 0$, $m = 1$). The waveguide ($n = 2.1$) is treated as an infinitely long rectangle (350 nm $\times$ 100 nm) supported by silica ($n = 1.45$) covered by either air ($n = 1.0$) or water ($n = 1.3$). The cutoff wavelength (when $n_{eff} = n_{substrate}$) for the $m = 1$ mode red shifts by $\sim$125 nm when the cover index is switched from air to water, which is in good agreement with the experimental data. The dispersion simulations were carried out using the MODE solutions software package (Lumerical Solutions, Inc.). Reproduced with permission. Copyright 2005 National Academy of Sciences, U.S.A.

and cross-bar grids have already been implemented in nanowire-based electronic logic,[31] which suggests that similar nanowire architectures could be potentially used in integrated optical logic[149−152] and all-optical switching.[153]

7.3. Waveguiding in Liquid Media. One advantage that high dielectric ($n \geq 2$) semiconductor wires and nanoribbons have over subwavelength silica waveguides[154] is their ability to efficiently transport light in water and other liquid media.[148] This becomes extremely important for applications such as on-chip chemical analysis or biological spectroscopy, which require small probe volumes. Figure 22a,b illustrates an interesting waveguiding effect observed when a thin ribbon (in this case, 265 μm $\times$ 365 nm $\times$ 105 nm) is immersed in water. The air ($n = 1$) cutoff wavelength (empirically determined from the spectrum, Figure 22c) is $\sim$483 nm, but shifts to the red ($\sim$570 nm) when the upper cladding is replaced by pure water ($n = 1.33$). This result would be anomalous for a step-index fiber that has a homogeneous dielectric cladding. In this case, one would expect the decrease in the refractive index mismatch between the core (ribbon) and cladding (water) to increase losses and cause a blue shift of the single mode cutoff wavelength. However, in air the waveguide is surrounded by an anisotropic cladding (i.e., where $n_{waveguide} > n_{substrate} > n_{cover}$), but changing the cover index to water creates a situation when the waveguide is surrounded by a nearly isotropic cladding. The reduction in cladding asymmetry decreases the amount of energy directed

into the substrate by allowing the radiation field to flow parallel to substrate.[155−157] Dispersion curves, relating the effective refractive index to wavelength, are plotted in Figure 22d. They show a definite red shift in the cutoff wavelength ($>$100 nm) of lower order guided modes ($m = 1$) as the cover index is changed from air to water, in good agreement with experiment. Ribbons too thick to show a single mode cutoff in the visible were unaffected by immersion in water.

Due to the appreciable electric field intensity that travels outside of the cavity, these subwavelength waveguides can be used as molecular sensors by means of either an emission or absorption scheme. In the former, nanoribbon waveguides guide light into a liquid medium. Any appropriate fluorophore that passes through the cone of scattered light, near the aperture of the waveguide, will be excited. This is demonstrated in Figure 23a by covering the end of ribbon waveguide (540 μm $\times$ 240 nm $\times$ 260 nm) with a small ($\sim$3 pL) droplet of 1,5-pentanediol ($n = 1.45$) loaded with 1 mM of rhodamine 6G laser dye (R6G). Blue light (442) launched into the opposite end of the ribbon produces strong fluorescence within the droplet, where the R6G maps out the ribbon's spatial emission pattern as a cone of light. Interestingly, a fraction of the R6G fluorescence is also captured by the ribbon cavity and routed back to the input end of the ribbon. This occurs only for the molecules that are in close proximity to the cavity, allowing both the direct and back-guided fluorescence to be probed (Figure 23b).
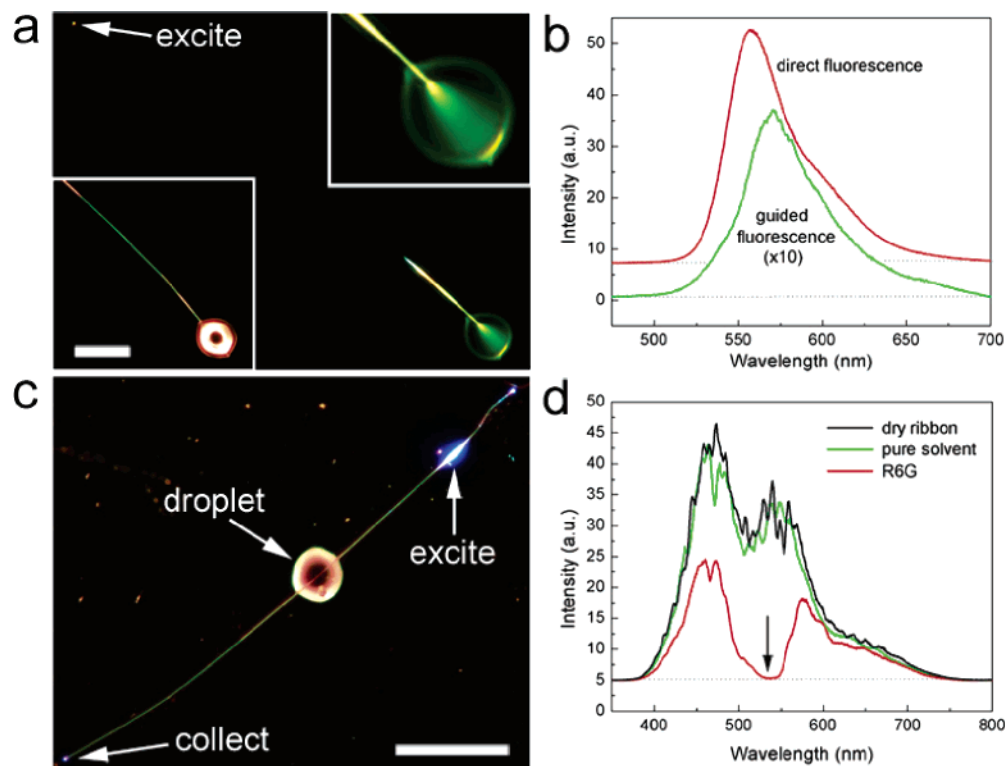
Figure 23. Demonstration of a fluorescence and absorption scheme using individual SnO_2 nanoribbon waveguides. (a) PL image of a ribbon (560 μm $\times$ 260 nm $\times$ 240 nm) immersed in a $\sim$3 pL 1,5-pentanediol droplet loaded with 1 mM R6G. Blue light (442 nm) is then launched down ribbon waveguide to excite R6G molecules in near proximity ($\sim$135 nm) to the cavity. Bottom inset: Dark-field image showing a zoom out of the ribbon's end immersed in the glycol droplet. Scale bar = 50 μm. Top inset: Magnified view of the R6G molecules being evanescently pumped along the length of the cavity and at the end as the blue light emanates out of the end terminus. (b) R6G spectra recorded directly over the droplet (red) and at the input terminus collecting the back guided fluorescence (green). The slight red shift is caused by an optical cavity effect (see ref 175). (c) Dark-field/PL image of the absorption scheme showing the analyte ($\sim$1 pL of R6G loaded glycol) centered in the middle of the ribbon (same ribbon as above) and the labeled excitation and collection locations. UV light was focused on the ribbon to generate white light that was launched through the 1 mM R6G loaded glycol. Scale bar = 100 μm. (d) Spectra recorded after the SnO_2 defect emission traversed through the ribbon in air (black), pure glycol (green), and 1 mM dye loaded glycol (red). The arrow denotes the absorption maximum ($\sim$535 nm) of R6G. Reproduced with permission. Copyright 2005 National Academy of Sciences, U.S.A.

The PL image in Figure 23a also shows strong fluorescence along the length of the ribbon, where the dye droplet has wet it by capillary action. The molecules close to waveguide surface are excited through a process similar to total internal reflection fluorescence (TIRF). In normal macroscopic TIRF, a waveguide (either a coverslip or dielectric strip) locally senses fluorophores via an evanescent field that decays exponentially with increasing distance from the waveguide surface,[158,159] giving a probe depth of $\sim$100 nm. Since subwavelength waveguides carry a larger percentage of their field intensity outside of the cavity ($\sim$15–25% for the ribbons used here), they increase the penetration depth of the field intensity into the cladding material, thereby intensifying the amount of power available to the nearby molecules.

An alternative sensing mechanism is to detect the light that is absorbed by molecules in close proximity to the waveguide surface. Although inherently less sensitive than fluorescence techniques (due to larger background signal), absorption spectroscopy is applicable to a variety of molecules and eliminates the need for tagging molecules with fluorophores. A broad light signal (i.e., white light) can be launched down the SnO_2 nanoribbon by exciting one end with UV light. If a small droplet is deposited on the cavity, it is possible to probe the resulting emission profile at the opposite end. This is demonstrated in Figure 23c,d, where a $\sim$1 pL glycol droplet loaded with 1 mM R6G was placed in the middle of a nanoribbon cavity. Figure 23d shows that the dye molecules imprint their absorption profile

on the propagating beam, completely quenching transmission near the absorption maximum of R6G ($\alpha_{max} = 535$ nm). The estimated probe volume for 600 nm light traveling through a 250 nm diameter cavity ($\sim$50 μm path length) is approximately 12 femtoliters. Considering the concentration of the dye, the ribbon is sensing less than forty attomoles of dye ($\sim$10^7 molecules) in this experiment. Future experiments should provide insight into the sensing limitation using subwavelength waveguides. Since the ribbon waveguides are acting as single pass detectors, simple improvements can be made to increase sensitivity, including decreasing the cross-sectional dimensions of the ribbon and changing the cavity shape to increase the path length. The natural directions for these novel fluidic sensors are to functionalize the ribbon surface for selective biosensing, design parallel sensing schemes, develop interferometry based sensors, and integrate them into microfluidic devices.[160] Last, since the nanoribbons are mechanically flexible probes and waveguide in any material of lesser refractive index, it should be possible to use them as internal light sources to investigate intracellular phenomena.

8. Concluding Remarks

Single-crystalline 1D structures are intriguing materials both for fundamental studies and future photonic applications. We have shown that chemically synthesized nanoribbons and nanowires offer a unique materials platform for producing key photonic elements including lasers, LEDs, detectors, and passive

Feature Article

J. Phys. Chem. B, Vol. 109, No. 32, 2005 **15211**

elements. The next step is to integrate them with existing photonic and sensing technologies to realize their full potential in future optoelectronic devices. Since the range of nanowire material types now include active, passive, nonlinear and semiconducting inorganic crystals, as well as a rich variety of polymers, synthesizing from the bottom up offers novel design-by-choice schemes to facilitate the assembly of multifunctioning components on the same substrate. Last, in comparison to their lithographically defined counterparts, which are permanently affixed to their substrates, chemically synthesized nanowires and nanoribbons are free-standing, mechanically flexible entities that can be integrated with microelectromechanical systems (MEMS) to further augment the study of physical and biological phenomena.

To capitalize on the novelty of nanomaterials, however, several issues must be resolved. First, the integration and parallel assembly of nanowire photonic elements into useful architectures needs to be solved. Devising reproducible physical or fluidic schemes to precisely move and position nanowire components on a device substrate will be central to the commercialization of nanoscale electronics and optics. Second, the power transfer efficiency between coupled nanowires is relatively low compared to monolithic structures defined by lithography. Developing synthetic approaches to producing branched structures, instead of assembling multicomponent devices, would be one way of reducing inter-wire losses. Last, geometric perfection, size dispersion, and shape control are issues for developing high Q-factor resonators and low-loss passive components. Without the precise control of these parameters it will be difficult to integrate these materials into future photonic and biological devices. Despite these current limitations, free-standing, chemically synthesized nanowires are clearly promising materials for the development of subwavelength photonics.

References and Notes

(1) Eldada, L. *Rev. Sci. Instrum.* **2004**, *75*, 575.
(2) Psaltis, D. *Science* **2002**, *298*, 1359.
(3) Joannopoulos, J. D.; Villeneuve, P. R.; Fan, S. H. *Nature* **1997**, *386*, 143.
(4) Lopez, C. *Adv. Mater.* **2003**, *15*, 1679.
(5) John, S. *Phys. Rev. Lett.* **1987**, *58*, 2486.
(6) Yablonovitch, E. *Phys. Rev. Lett.* **1987**, *58*, 2059.
(7) Noda, S.; Tomoda, K.; Yamamoto, N.; Chutinan, A. *Science* **2000**, *289*, 604.
(8) Quidant, R.; Weeber, J. C.; Dereux, A.; Peyrade, D.; des Francs, G. C.; Girard, C.; Chen, Y. *Phys. Rev. E* **2001**, *64*.
(9) Barnes, W. L.; Dereux, A.; Ebbesen, T. W. *Nature* **2003**, *424*, 824.
(10) Maier, S. A.; Kik, P. G.; Atwater, H. A.; Meltzer, S.; Harel, E.; Koel, B. E.; Requicha, A. A. G. *Nat. Mater.* **2003**, *2*, 229.
(11) Krenn, J. R.; Weeber, J. C. *Philos. Trans. R. Soc. London, Ser. A* **2004**, *362*, 739.
(12) Alivisatos, A. P. *Science* **1996**, *271*, 933.
(13) Brus, L. *Appl. Phys. A* **1991**, *53*, 465.
(14) Murray, C. B.; Norris, D. J.; Bawendi, M. G. *J. Am. Chem. Soc.* **1993**, *115*, 8706.
(15) Yoffe, A. D. *Adv. Phys.* **2001**, *50*, 1.
(16) Someya, T.; Werner, R.; Forchel, A.; Catalano, M.; Cingolani, R.; Arakawa, Y. *Science* **1999**, *285*, 1905.
(17) Gerard, J. M.; Sermage, B.; Gayral, B.; Legrand, B.; Costard, E.; Thierry-Mieg, V. *Phys. Rev. Lett.* **1998**, *81*, 1110.
(18) Tanaka, K.; Nakamura, T.; Takamatsu, W.; Yamanishi, M.; Lee, Y.; Ishihara, T. *Phys. Rev. Lett.* **1995**, *74*, 3380.
(19) Nag, B. R. *Physics of Quantum Well Devices*; Kluwer: Dordrecht, The Netherlands, 2000.
(20) Wang, Z. L. *Adv. Mater.* **2000**, *12*, 1295.
(21) Yang, P. *MRS Bull.* **2005**, *30*, 85.
(22) Hu, J. T.; Odom, T. W.; Lieber, C. M. *Acc. Chem. Res.* **1999**, *32*, 435.
(23) Cerrina, F.; Marian, C. *MRS Bull.* **1996**, *21*, 56.
(24) Gibson, J. M. *Phys. Today* **1997**, *50*, 56.
(25) Matsui, S.; Ochiai, Y. *Nanotechnol.* **1996**, *7*, 247.
(26) Hong, S. H.; Zhu, J.; Mirkin, C. A. *Science* **1999**, *286*, 523.
(27) Dagata, J. A. *Science* **1995**, *270*, 1625.
(28) Levenson, M. D. *Solid State Technol.* **1995**, *38*, 81.
(29) Dunn, P. N. *Solid State Technol.* **1994**, *37*, 49.
(30) Xia, Y. N.; Yang, P. D.; Sun, Y. G.; Wu, Y. Y.; Mayers, B.; Gates, B.; Yin, Y. D.; Kim, F.; Yan, Y. Q. *Adv. Mater.* **2003**, *15*, 353.
(31) Huang, Y.; Duan, X. F.; Cui, Y.; Lauhon, L. J.; Kim, K. H.; Lieber, C. M. *Science* **2001**, *294*, 1313.
(32) Cui, Y.; Lieber, C. M. *Science* **2001**, *291*, 851.
(33) Duan, X. F.; Huang, Y.; Cui, Y.; Wang, J. F.; Lieber, C. M. *Nature* **2001**, *409*, 66.
(34) Wang, J. F.; Gudiksen, M. S.; Duan, X. F.; Cui, Y.; Lieber, C. M. *Science* **2001**, *293*, 1455.
(35) Kind, H.; Yan, H. Q.; Messer, B.; Law, M.; Yang, P. D. *Adv. Mater.* **2002**, *14*, 158.
(36) Law, M.; Kind, H.; Messer, B.; Kim, F.; Yang, P. D. *Angew. Chem., Int. Ed. Engl.* **2002**, *41*, 2405.
(37) Qian, F.; Li, Y.; Gradecak, S.; Wang, D.; Barrelet, C. J.; Lieber, C. M. *Nano Lett.* **2004**, *4*, 1975.
(38) Choi, H.-J.; Seong, H.-K.; Chang, J.; Lee, K.-I.; Park, Y.-J.; Kim, J.-J.; Lee, S.-K.; He, R.; Kuykendall, T.; Yang, P. *Adv. Mater.* **2005**, *17*, 1351.
(39) Gudiksen, M. S.; Lauhon, L. J.; Wang, J.; Smith, D. C.; Lieber, C. M. *Nature* **2002**, *415*, 617.
(40) Huang, Y.; Duan, X. F.; Lieber, C. M. *Small* **2005**, *1*, 142.
(41) Huang, M. H.; Mao, S.; Feick, H.; Yan, H. Q.; Wu, Y. Y.; Kind, H.; Weber, E.; Russo, R.; Yang, P. D. *Science* **2001**, *292*, 1897.
(42) Duan, X. F.; Huang, Y.; Agarwal, R.; Lieber, C. M. *Nature* **2003**, *421*, 241.
(43) Yang, P. D.; Yan, H. Q.; Mao, S.; Russo, R.; Johnson, J.; Saykally, R.; Morris, N.; Pham, J.; He, R. R.; Choi, H. J. *Adv. Funct. Mater.* **2002**, *12*, 323.
(44) Huang, M. H.; Wu, Y. Y.; Feick, H.; Tran, N.; Weber, E.; Yang, P. D. *Adv. Mater.* **2001**, *13*, 113.
(45) Yan, H. Q.; He, R. R.; Johnson, J.; Law, M.; Saykally, R. J.; Yang, P. D. *J. Am. Chem. Soc.* **2003**, *125*, 4728.
(46) Kuykendall, T.; Pauzauskie, P.; Lee, S. K.; Zhang, Y.; Yang, P. *Nano Lett.* **2003**, *3*, 1063.
(47) Johnson, J. C.; Choi, H. J.; Knutsen, K. P.; Schaller, R. D.; Yang, P. D.; Saykally, R. J. *Nat. Mater.* **2002**, *1*, 106.
(48) Pan, Z. W.; Dai, Z. R.; Wang, Z. L. *Science* **2001**, *291*, 1947.
(49) Johnson, J. C.; Knutsen, K. P.; Yan, H. Q.; Law, M.; Zhang, Y. F.; Yang, P. D.; Saykally, R. J. *Nano Lett.* **2004**, *4*, 197.
(50) Schaller, R. D.; Johnson, J. C.; Wilson, K. R.; Lee, L. F.; Haber, L. H.; Saykally, R. J. *J. Phys. Chem. B* **2002**, *106*, 5143.
(51) Givargizov, E. I. *Highly Anisotropic Crystals*; Reidel: Dordrecht, The Netherlands, 1987.
(52) Wagner, R. S.; Ellis, W. C. *Appl. Phys. Lett.* **1964**, *4*, 89.
(53) Chen, C. C.; Yeh, C. C. *Adv. Mater.* **2000**, *12*, 738.
(54) Chen, C. C.; Yeh, C. C.; Chen, C. H.; Yu, M. Y.; Liu, H. L.; Wu, J. J.; Chen, K. H.; Chen, L. C.; Peng, J. Y.; Chen, Y. F. *J. Am. Chem. Soc.* **2001**, *123*, 2791.
(55) Chen, Y. J.; Li, J. B.; Han, Y. S.; Yang, X. Z.; Dai, J. H. *J. Cryst. Growth* **2002**, *245*, 163.
(56) Duan, X. F.; Lieber, C. M. *Adv. Mater.* **2000**, *12*, 298.
(57) Duan, X. F.; Lieber, C. M. *J. Am. Chem. Soc.* **2000**, *122*, 188.
(58) He, M. Q.; Zhou, P. Z.; Mohammad, S. N.; Harris, G. L.; Halpern, J. B.; Jacobs, R.; Sarney, W. L.; Salamanca-Riba, L. *J. Cryst. Growth* **2001**, *231*, 357.
(59) Katsuyama, T.; Hiruma, K.; Ogawa, K.; Haraguchi, K.; Yazawa, M. *Jpn. J. Appl. Phys., Part 2* **1994**, *34*, 224.
(60) Lopez-Lopez, M.; Guillen-Cervantes, A.; Rivera-Alvarez, Z.; Hernandez-Calderon, I. *J. Cryst. Growth* **1998**, *193*, 528.
(61) Miyao, M.; Nakagawa, K.; Ichikawa, M.; Hiruma, K.; Nakazato, K. *Jpn. J. Appl. Phys., Part 1* **1994**, *33*, 7214.
(62) Morales, A. M.; Lieber, C. M. *Science* **1998**, *279*, 208.
(63) Pan, Z. W.; Lai, H. L.; Au, F. C. K.; Duan, X. F.; Zhou, W. Y.; Shi, W. S.; Wang, N.; Lee, C. S.; Wong, N. B.; Lee, S. T.; Xie, S. S. *Adv. Mater.* **2000**, *12*, 1186.

(64) Yang, P.; Wu, Y. *J. Am. Chem. Soc.* **2001**, *123*, 3165.

(65) Wu, Y.; Law, M.; Messer, B.; Kind, H.; Yang, P. *Adv. Mater.* **2001**, *19*, 1487.

(66) Wu, Y.; Fan, R.; Yang, P. *Nano Lett.* **2002**, *2*, 83.

(67) Westwater, J.; Gosain, D. P.; Tomiya, S.; Usui, S.; Ruda, H. *J. Vac. Sci. Technol. B* **1997**, *15*, 554.

(68) Stach, E.; Pauzauskie, P.; Kuykendall, T.; Goldberger, J.; Yang, P. *Nano. Lett.* **2003**, *3*, 867.

(69) Wu, X. C.; Song, W. H.; Zhao, B.; Sun, Y. P.; Du, J. J. *Chem. Phys. Lett.* **2001**, *349*, 210.

(70) Wu, Y. Y.; Yang, P. D. *Chem. Mater.* **2000**, *12*, 605.

(71) Yazawa, M.; Koguchi, M.; Muto, A.; Hiruma, K. *Adv. Mater.* **1993**, *5*, 577.

(72) Zhang, J.; Peng, X. S.; Wang, X. F.; Wang, Y. W.; Zhang, L. D. *Chem. Phys. Lett.* **2001**, *345*, 372.

(73) Zhang, Y. J.; Zhang, Q.; Wang, N. L.; Yan, Y. J.; Zhou, H. H.; Zhu, J. *J. Cryst. Growth* **2001**, *226*, 185.

(74) Hiruma, K.; Yazawa, M.; Katsuyama, T.; Ogawa, K.; Haraguchi, K.; Koguchi, M.; Kakibayashi, H. *J. Appl. Phys.* **1995**, *5*, 577.

(75) Shimada, T.; Hiruma, K.; Shirai, M.; Yazawa, M.; Haraguchi, K.; Sato, T.; Matsui, M.; Katsuyama, T. *Superlatt. Microstruct.* **1998**, *24*, 453.

(76) Law, M.; Goldberger, J.; Yang, P. D. *Annu. Rev. Mater. Sci.* **2004**, *34*, 84.

(77) Martensson, T.; Carlberg, P.; Borgstrom, M.; Montelius, L.; Seifert, W.; Samuelson, L. *Nano Lett.* **2004**, *4*, 699.

(78) Han, S.; Jin, W.; Tang, T.; Li, C.; Zhang, D. H.; Liu, X. L.; Han, J.; Zhou, C. W. *J. Mater. Res.* **2003**, *18*, 245.

(79) Ohlsson, B. J.; Bjork, M. T.; Magnusson, M. H.; Deppert, K.; Samuelson, L.; Wallenberg, L. R. *Appl. Phys. Lett.* **2001**, *79*, 3335.

(80) Holmes, J. D.; Johnston, K. P.; Doty, R. C.; Korgel, B. A. *Science* **2000**, *287*, 1471.

(81) Haraguchi, K.; Hiruma, K.; Katsuyama, T.; Tominaga, K.; Shirai, M.; Shimada, T. *Appl. Phys. Lett.* **1996**, *69*, 386.

(82) Wu, Y. Y.; Yan, H. Q.; Huang, M.; Messer, B.; Song, J. H.; Yang, P. D. *Chem.− A Eur. J.* **2002**, *8*, 1261.

(83) Kuykendall, T.; Pauzauskie, P. J.; Zhang, Y. F.; Goldberger, J.; Sirbuly, D.; Denlinger, J.; Yang, P. D. *Nat. Mater.* **2004**, *3*, 524.

(84) Park, W. I.; Yi, G. C.; Kim, M.; Pennycook, S. J. *Adv. Mater.* **2003**, *15*, 526.

(85) Reynolds, D. C.; Look, D. C.; Jogai, B.; Litton, C. W.; Collins, T. C.; Harsch, W.; Cantwell, G. *Phys. Rev. B* **1998**, *57*, 12151.

(86) Park, W. I.; An, S. J.; Yi, G. C.; Jang, H. M. *J. Mater. Res.* **2001**, *16*, 1358.

(87) Jung, S. W.; Park, W. I.; Cheong, H. D.; Yi, G. C.; Jang, H. M.; Hong, S.; Joo, T. *Appl. Phys. Lett.* **2002**, *80*, 1924.

(88) Park, W. I.; Jun, Y. H.; Jung, S. W.; Yi, G. C. *Appl. Phys. Lett.* **2003**, *82*, 964.

(89) Wang, D.; Liu, Y. C.; Mu, R.; Zhang, J. Y.; Lu, Y. M.; Shen, D. Z.; Fan, X. W. *J. Phys.: Condens. Matter* **2004**, *16*, 4635.

(90) Sun, Y. J.; Brandt, O.; Jahn, U.; Liu, T. Y.; Trampert, A.; Cronenberg, S.; Dhar, S.; Ploog, K. H. *J. Appl. Phys.* **2002**, *92*, 5714.

(91) Reynolds, D. C.; Look, D. C.; Jogai, B.; Litton, C. W.; Cantwell, G.; Harsch, W. C. *Phys. Rev. B* **1999**, *60*, 2340.

(92) Thomas, D. G. *J. Phys.* **1960**, *15*, 86.

(93) Hopfield, J. J. *J. Phys. Chem. Solids* **1960**, *15*, 97.

(94) Dean, P. J.; Cuthbert, J. D.; Thomas, D. G.; Lynch, R. T. *Phys. Rev. Lett.* **1967**, *18*, 122.

(95) Varshni, Y. P. *Physica* **1967**, *34*, 149.

(96) Studenikin, S. A.; Cocivera, M. *J. Appl. Phys.* **2002**, *91*, 5060.

(97) Egelhaaf, H. J.; Oelkrug, D. *J. Cryst. Growth* **1996**, *161*, 190.

(98) Vanheusden, K.; Warren, W. L.; Seager, C. H.; Tallant, D. R.; Voigt, J. A.; Gnade, B. E. *J. Appl. Phys.* **1996**, *79*, 7983.

(99) Snyder, A. W.; Love, J. D. *Optical Waveguide Theory*; Chapman and Hall: London, 1983.

(100) Glinka, Y. D.; Shahbazyan, T. V.; Perakis, I. E.; Tolk, N. H.; Liu, X.; Sasaki, Y.; Furdyna, J. K. *Appl. Phys. Lett.* **2002**, *81*, 3717.

(101) Mikhailovsky, A. A.; Malko, A. V.; Hollingsworth, J. A.; Bawendi, M. G.; Klimov, V. I. *Appl. Phys. Lett.* **2002**, *80*, 2380.

(102) Johnson, J. C.; Yan, H. Q.; Yang, P. D.; Saykally, R. J. *J. Phys. Chem. B* **2003**, *107*, 8816.

(103) Johnson, J. C.; Yan, H. Q.; Schaller, R. D.; Haber, L. H.; Saykally, R. J.; Yang, P. D. *J. Phys. Chem. B* **2001**, *105*, 11387.

(104) Guo, B.; Qiu, Z. R.; Wong, K. S. *Appl. Phys. Lett.* **2003**, *82*, 2290.

(105) Takeda, J.; Jinnouchi, H.; Kurita, S.; Chen, Y. F.; Yao, T. *Phys. Status Solidi B* **2002**, *229*, 877.

(106) Zhang, W. L.; Chai, L.; Xing, Q. R.; Wang, Q. Y.; Wong, K. S.; Yu, P.; Wang, H.; Tang, Z. K.; Wong, G. K. L. *Chin. Phys. Lett.* **1999**, *16*, 728.

(107) Yamamoto, A.; Kido, T.; Goto, Y. F.; Chen, Y.; Yao, T.; Kasuya, A. *Appl. Phys. Lett.* **1999**, *75*, 469.

(108) Fujino, T.; Tahara, T. *J. Phys. Chem. B* **2003**, *107*, 5120.

(109) Yoshikawa, H.; Sasaki, K.; Masuhara, H. *Chem. Phys. Lett.* **1998**, *293*, 185.

(110) Guo, B.; Ye, Z. Z.; Wong, K. S. *J. Cryst. Growth* **2003**, *253*, 252.

(111) Yamamoto, A.; Kido, T.; Goto, T.; Chen, Y. F.; Yao, T. F.; Kasuya, A. *J. Cryst. Growth* **2000**, *214*, 308.

(112) Johnson, J. C.; Yan, H.; Schaller, R. D.; Peterson, P. B.; Yang, P.; Saykally, R. J. *Nano Lett.* **2002**, *2*, 279.

(113) Schaller, R. D.; Johnson, J. C.; Saykally, R. J. *ChemPhysChem* **2003**, *4*, 1243.

(114) Maslov, A. V.; Ning, C. Z. *Appl. Phys. Lett.* **2003**, *83*, 1237.

(115) Maslov, A. V.; Ning, C. Z. *Opt. Lett.* **2004**, *29*, 572.

(116) Maslov, A. V.; Ning, C. Z. *IEEE J. Quantum Electron.* **2004**, *40*, 1389.

(117) Bagnall, D. M.; Chen, Y. F.; Zhu, Z.; Yao, T.; Koyama, S.; Shen, M. Y.; Goto, T. *Appl. Phys. Lett.* **1997**, *70*, 2230.

(118) Cao, H.; Zhao, Y. G.; Ong, H. C.; Ho, S. T.; Dai, J. Y.; Wu, J. Y.; Chang, R. P. H. *Appl. Phys. Lett.* **1998**, *73*, 3656.

(119) Sun, Y.; Ketterson, J. B.; Wong, G. K. L. *Appl. Phys. Lett.* **2000**, *77*, 2322.

(120) Bagnall, D. M.; Chen, Y. F.; Shen, M. Y.; Zhu, Z.; Goto, T.; Yao, T. *J. Cryst. Growth* **1998**, *185*, 605.

(121) Klingshirn, C. *Optical Properties of Semiconductors*; Springer: New York, 1995.

(122) Bidnyk, S.; Schmidt, T. J.; Little, B. D.; Song, J. J. *Appl. Phys. Lett.* **1999**, *74*, 1.

(123) Svelto, O. *Principles of Lasers*; Plenum: New York, 1998.

(124) Chang, S. S.; Rex, N. B.; Chang, R. K.; Chong, G.; Guido, L. J. *Appl. Phys. Lett.* **1999**, *75*, 166.

(125) Sun, X. W.; Kwok, H. S. *J. Appl. Phys.* **1999**, *86*, 408.

(126) Domen, K.; Kondo, K.; Kuramata, A.; Tanahashi, T. *Appl. Phys. Lett.* **1996**, *69*, 94.

(127) Chen, Y. F.; Tuan, N. T.; Segawa, Y.; Ko, H.; Hong, S.; Yao, T. *Appl. Phys. Lett.* **2001**, *78*, 1469.

(128) Tang, Z. K.; Wong, G. K. L.; Yu, P.; Kawasaki, M.; Ohtomo, A.; Koinuma, H.; Segawa, Y. *Appl. Phys. Lett.* **1998**, *72*, 3270.

(129) Maslov, A. V.; Ning, C. Z. *Proc. SPIE* **2004**, *5349*, 24.

(130) Lieber, C. M. *Solid State Commun.* **1998**, *107*, 607.

(131) Yan, H. Q.; He, R. R.; Pham, J.; Yang, P. D. *Adv. Mater.* **2003**, *15*, 402.

(132) Yan, H. Q.; Johnson, J.; Law, M.; He, R. R.; Knutsen, K.; McKinney, J. R.; Pham, J.; Saykally, R.; Yang, P. D. *Adv. Mater.* **2003**, *15*, 1907.

(133) Choi, H.; Johnson, J.; He, R.; Lee, S.; Kim, F.; Pauzauskie, P.; Goldberger, J.; Saykally, R.; Yang, P. *J. Phys. Chem. B* **2003**, *107*, 8721.

(134) Tans, S. J.; Verschueren, A. R. M.; Dekker, C. *Nature* **1998**, *393*, 49.

(135) Martel, R.; Schmidt, T.; Shea, H. R.; Hertel, T.; Avouris, Ph. *Appl. Phys. Lett.* **1998**, *73*, 2447.

(136) Dekker, C. *Phys. Today* **1999**, *52*, 22.

(137) Tseng, G. Y.; Ellenbogen, J. C. *Science* **2001**, *294*, 1293.

(138) Cobden, D. H. *Nature* **2001**, *409*, 32.

(139) Service, R. F. *Science* **2001**, *293*, 782.

(140) Rose, A. *Concepts in Photoconductivity and Allied Problems*; Krieger: New York, 1978.

(141) Takahashi, Y.; Kanamori, M.; Kondoh, A.; Minoura, H.; Ohya, Y. *Jpn. J. Appl. Phys.* **1994**, *33*, 6611.

(142) Liu, Y.; Gorla, C. R.; Liang, S.; Emanetoglu, N.; Lu, Y.; Shen, H.; Wraback, M. *J. Electron. Mater.* **2000**, *29*, 69.

(143) Goldberger, J.; Sirbuly, D. J.; Law, M.; Yang, P. *J. Phys. Chem. B* **2005**, *109*, 9.

(144) Almeida, V. R.; Xu, Q. F.; Barrios, C. A.; Lipson, M. *Opt. Lett.* **2004**, *29*, 1209.

(145) Law, M.; Sirbuly, D. J.; Johnson, J. C.; Goldberger, J.; Saykally, R. J.; Yang, P. D. *Science* **2004**, *305*, 1269.

(146) Reddick, R. C.; Warmack, R. J.; Chilcott, D. W.; Sharp, S. L.; Ferrell, T. L. *Rev. Sci. Instrum.* **1990**, *61*, 3669.

(147) López, C. *Small* **2005**, *1*, 378.

(148) Sirbuly, D. J.; Law, M.; Pauzauskie, P.; Yan, H.; Maslov, A. V.; Knutsen, K.; Ning, C. Z.; Saykally, R. J.; Yang, P. *Proc. Natl. Acad. Sci. U.S.A.* **2005**, *102*, 1800.

(149) Tominaga, J.; Mihalcea, C.; Buchel, D.; Fukuda, H.; Nakano, T.; Atoda, N.; Fuji, H.; Kikukawa, T. *Appl. Phys. Lett.* **2001**, *78*, 2417.

(150) Christodoulides, D. N.; Lederer, F.; Silberberg, Y. *Nature* **2003**, *424*, 817.

(151) O'Brien, J. L.; Pryde, G. J.; White, A. G.; Ralph, T. C.; Branning, D. *Nature* **2003**, *426*, 264.

(152) Paniccia, N.; Morse, M.; Salib, M. Integrated photonics. In *Silicon Photonics*, 2004; Vol. 94; p 51.

Feature Article

J. Phys. Chem. B, Vol. 109, No. 32, 2005 **15213**

(153) Ibrahim, T. A.; Cao, W.; Kim, Y.; Li, J.; Goldhar, J.; Ho, P. T.; Lee, C. H. *IEEE Photonics Technol. Lett.* **2003**, *15*, 36.

(154) Tong, L. M.; Gattass, R. R.; Ashcom, J. B.; He, S. L.; Lou, J. Y.; Shen, M. Y.; Maxwell, I.; Mazur, E. *Nature* **2003**, *426*, 816.

(155) Wakita, K. *Semiconductor Optical Modulators*; Kluwer Academic Publishers: Boston, 1998.

(156) Kogelnik, H.; Ramaswam, V. *Appl. Opt.* **1974**, *13*, 1857.

(157) Klunder, D. J. W.; Tan, F. S.; van der Veen, T.; Bulthuis, H. F.; Sengo, G.; Docter, B.; Hokstra, H.; Driessen, A. *J. Lightwave Technol.* **2003**, *21*, 1099.

(158) Stephens, D. J.; Allan, V. J. *Science* **2003**, *300*, 82.

(159) Sund, S. E.; Axelrod, D. *Biophys. J.* **2000**, *79*, 1655.

(160) Petersen, N. J.; Mogensen, K. B.; Kutter, J. P. *Electrophoresis* **2002**, *23*, 3528.